

Quantitative phase-field modeling for wetting phenomena

Arnoldo Badillo*

Thermal-Hydraulics Laboratory, Paul Scherrer Institute, CH-5232 Villigen PSI, Switzerland

(Received 26 November 2014; published 6 March 2015)

A new phase-field model is developed for studying partial wetting. The introduction of a third phase representing a solid wall allows for the derivation of a new surface tension force that accounts for energy changes at the contact line. In contrast to other multi-phase-field formulations, the present model does not need the introduction of surface energies for the fluid-wall interactions. Instead, all wetting properties are included in a unique parameter known as the equilibrium contact angle θ_{eq} . The model requires the solution of a single elliptic phase-field equation, which, coupled to conservation laws for mass and linear momentum, admits the existence of steady and unsteady compact solutions (compactons). The representation of the wall by an additional phase field allows for the study of wetting phenomena on flat, rough, or patterned surfaces in a straightforward manner. The model contains only two free parameters, a measure of interface thickness W and β , which is used in the definition of the mixture viscosity $\mu = \mu_l\phi_l + \mu_v\phi_v + \beta\mu_w\phi_w$. The former controls the convergence towards the sharp interface limit and the latter the energy dissipation at the contact line. Simulations on rough surfaces show that by taking values for β higher than 1, the model can reproduce, on average, the effects of pinning events of the contact line during its dynamic motion. The model is able to capture, in good agreement with experimental observations, many physical phenomena fundamental to wetting science, such as the wetting transition on micro-structured surfaces and droplet dynamics on solid substrates.

DOI: 10.1103/PhysRevE.91.033005

PACS number(s): 47.55.np, 68.03.Cd, 68.08.Bc

I. INTRODUCTION

How to represent mathematically the physics behind wetting phenomena has been the main topic of countless publications, where each of them has contributed with one step forward to a better understanding of this challenging problem. Nonetheless, and despite these efforts, we are still unable to develop a theory capable of predicting all the experimental observations. At the molecular level, atomic interactions are quite complex, but theories usually must consider oversimplified interatomic potentials to cope with the mathematics required to solve the problem. In a recent review written by Bonn *et al.* [1], it was shown that current molecular theories represent interatomic interactions by a Lennard-Jones potential, plus corrections due to other forces such as electrostatic interactions. Despite the fact that these phenomenological potentials can predict many of the physical properties of fluids in the range of temperatures and pressures for which they were fitted, it is not possible to predict all of them simultaneously with a unique potential. A good example of this are the potentials developed for water, where different ones must be used for accurate calculations of the phase diagram, surface tension, radial distribution, and many other properties. Pair additivity of the atomic interactions is always used to calculate the Hamiltonian and circumvent the many-body problem, but, by doing so, several degrees of freedom are smoothed out and information of higher-order correlations is lost. Then one might wonder if efforts to develop a new molecular theory of wetting, which consider three phases in contact, are justified if the liquid-vapor interface is still not accurately described by current theories.

At macroscales we are not exempted from difficulties. For instance, wetting models based on conventional

hydrodynamics suffer from the stress singularity at the contact line. For more details about macroscopic models for wetting phenomena, the reader is referred to a recent review written by Sui *et al.* [2]. To sort out the stress singularity at the contact line, Cox [3] postulated that a certain amount of slip must occur in the nearby region of the contact line. By means of perturbation theory, he derived a well-known expression to relate the apparent (dynamic) contact angle with the slip velocity at the contact line and the equilibrium contact angle. From a traditional hydrodynamic point of view, a certain amount of slip in the vicinity of the contact line goes against the nonslip condition usually used at the fluid-wall interface. Nonetheless, a “traditional” hydrodynamic analysis involves only two-phase flows (fluid-solid), but at the contact line we have an additional degree of freedom that must be accounted for (a third phase). Qian *et al.* [4,5] used molecular dynamic simulations to study the local stress field at the contact line. The simulations showed that far from the contact line the slip velocity was negligible, in agreement with the nonslip condition. Nevertheless, a sharply peaked slip velocity distribution was observed in the vicinity of the contact line. They explained the slip velocity in terms of an unbalanced stress tensor in the proximity of a moving contact line, which arises from the deviation of the apparent contact angle from the thermodynamic one (equilibrium contact angle). They also showed that the slip velocity was linearly proportional to the force originating on the unbalanced capillary stress tensor (Young stress in their definition). These results have certainly improved our understanding of the dynamics inherent to moving contact lines, but the extrapolation of this knowledge to real systems requires the development of new models.

Several phase-field models have already been derived for wetting phenomena (see Anderson *et al.* [6] for a review on diffuse interface methods in fluid dynamics and Seppecher [7] for an early treatment of moving contact lines in the Cahn-Hilliard framework). In these models the

*arnoldo.badillo@psi.ch

fluid-wall interactions are introduced either by suitable boundary condition [4,5,7–14] or by the use of a third phase field with a very high viscosity to represent a solid wall [15–21]. In this work I have chosen the second approach but with a substantial different definition of the free-energy functional. Multi-phase-field models (more than two phases) derived for eutectic solidification [22,23] can handle the evolution of several fields simultaneously, including triple junctions (the intersection of three phases). Villanueva *et al.* [15–17] and Wheeler *et al.* [18] followed the same principles to derive new models for reactive wetting, where the motion of the contact line is controlled by diffusion of species and capillary effects. In these models, the substrate is allowed to dissolve and consequently there is no guarantee that the system will relax towards the equilibrium contact angle given by the Young's equation. In spite of the fructiferous research on phase-field modeling of wetting phenomena, a comprehensive quantitative validation against experimental data is rarely presented. Yue and Feng [9] used a hydrodynamic Cahn-Hilliard model to predict the advancing contact angle as a function of the capillary number **Ca**, but good agreement with experiments was only achieved by adjusting a phenomenological parameter (Π), which has no clear connection to any physical property. Cueto-Felgueroso and Juanes [8] simulated the evolution of a liquid meniscus in a capillary tube during air injection. They compared the mass fraction of liquid left behind in the tube, but, once again, a fair agreement with experimental data for high **Ca** was achieved by choosing an unphysical contact angle ($\theta_{eq} = 180^\circ$) and by adjusting the dependence of the water mobility on the water saturation (there was no physical argument on how to determine this parameter). For low **Ca**, the agreement was less satisfactory even after modifying the water mobility. Since in this model wetting is considered to be driven by diffusion (where in the absence of external flow velocity u_T the water saturation only evolves by virtue of the gradient of the chemical potential), the best agreement should be achieved for low **Ca**. Nonetheless, it appears that a better agreement with experiments would require yet another dependence of the water mobility with the water saturation. Queralt-Martín *et al.* [12] study experimentally the advancement of a water front in a microchannel composed by two parallel plates with natural roughness (no manipulation of the surface after fabrication). They adjusted the pressure drop in the channel and found that for low values, the water front advances proportionally to $h(t) \propto t^\nu$ with $\nu = 0.38$, which is lower than the value of 0.5 predicted by the Washburn model. They attributed this lower exponent to pinning events at the contact line and to test their hypothesis, they used a two-dimensional Cahn-Hilliard model to study the pinning effects in a microchannel, with steps on the wall to resemble a surface roughness. They found that their model predicts an exponent close to 0.5 and 0.4 for high- and low-pressure differences, respectively. They also found that their model was able to predict a BHP-Gumbel distribution for the velocity fluctuations of the water front, which is consistent with their experimental observations. In spite of the interesting results, the comparison was only qualitative and the reason for the lower experimental exponent for low pressures drops is still not fully understood. In their experiment, the water front only moves a few millimeters over a time span of few hours. Since the experiment was not performed in a chamber

with controlled atmosphere, evaporation phenomena could have an important effect on the interface dynamics. In fact, for a null pressure difference, the interface should recede in an experiment performed at atmospheric conditions. Wheeler *et al.* [18] simulated the spreading of a molten drop on a solid substrate, showing a qualitative good agreement between their simulations and experimental results for two molten metals.

To circumvent a lack of validation, a great emphasis was placed on direct comparison between numerical simulations and experiments. In contrast to diffuse interface models where the equilibrium contact angle θ_{eq} is introduced in the natural boundary condition proposed by Cahn [14] or its kinematic version proposed by Qian *et al.* [4,5], the equilibrium contact angle is accounted for in the newly derived volumetric surface tension force. This force reduces to the standard expression derived in phase-field formulations far from the solid surface [4,24], but it varies sharply close to the contact line. When the dynamic apparent contact angle θ_d differs from the thermodynamic one θ_{eq} , a net force arises at the contact line inducing a velocity field, which forces the contact line to move in the direction that minimizes the difference $\Delta_\theta = \theta_{eq} - \theta_d$. The contact line thus relaxes towards the equilibrium configuration by advection and its rate of relaxation is only controlled by viscous dissipation near the contact line. This is the key feature that sets this model apart from those using the Cahn boundary condition [12,25] or its kinematic version [4,5] (see Ref. [26] for the influence of using either of these boundary conditions), where the contact line relaxes towards equilibrium by diffusion in the former case and by a nonconservative hydrodynamic Allen-Cahn equation in the latter. In addition, the use of a third phase (solid wall ϕ_w) facilitates direct numerical simulations of complex phenomena, such as conjugate heat transfer and moving solid walls (e.g., colloidal particles attached to the liquid-vapor interface).

This paper is organized as follows. The constitutive set of equations is presented in Sec. II. The meaning of surface tension (interface property) and the derivation of the new surface tension force are presented in Sec. III. To keep interface thickness constant and avoid the diffusion current employed in hydrodynamic Cahn-Hilliard models, the use of a new resharpening equation is discussed in Sec. IV. The assessment of the model to reproduce equilibrium phenomena, such as the wetting transition and the equilibrium contact angle for sessile drops on flat surfaces, is presented in Sec. V. The main objective of this work is to present a new quantitative formulation, which is general enough to be used in the study of many problems encountered in wetting science. Hence, a stringent comparison with experimental results plays a fundamental role in the assessment of the quantitative capabilities of the model. To this end, in Sec. VI three quite distinctive dynamic cases are addressed: First, the spreading of a drop on a flat surface is analyzed, where characteristic exponents for spreading rates in the intertial and dissipation controlled regimes are computed and compared to those from experimental observations. Second, we evaluate the influence of surface roughness, inclination angle, and β (used in the definition of the mixture viscosity) on the velocity of single droplets sliding down an inclined surface. Finally, the highly dynamic case of a drop impacting on a solid wall is studied, where a direct comparison between simulated and

measured contact area and dynamic contact angle is presented. Conclusions are presented in Sec. VII.

II. THE MODEL

The present model is the first step towards a quantitative phase-field description for wetting phenomena, which aims to predict the dynamics of contacts lines under several conditions. A big effort was spent to derive a model that reduces the excessive number of phenomenological parameters commonly used in phase-field approaches. From a personal point of view, phenomenological constants are the easiest way to hide our lack of knowledge of physics, and therefore, efforts should be made to avoid them whenever is possible or to provide a clear connection with physical properties. Although phase change (e.g., evaporation or condensation) is virtually present in all wetting phenomena, the current model neglects these effects and therefore is applicable to cases where capillary effects dominate the dynamics of the contact line and that of the liquid-vapor interface. Results concerning cases where phase change and conjugate heat transfer cannot be neglected (e.g., boiling and Leidenfrost phenomena) will be presented in a forthcoming publication, where the current model will be coupled to a quantitative phase-field model for boiling phenomena [24].

The current model is composed by conservation of mass and linear momentum and a re-sharpening equation to keep the interface thickness constant during its advection. Capillarity phenomena are treated by a unique surface tension force, which depends on a modified transformation potential to account for the presence of a solid surface. The wall is modeled with an additional phase field but with no surface energy associated to it.

A. Conservation laws

Assuming a stationary control volume, mass conservation for pure systems states

$$\frac{\partial \rho}{\partial t} + \nabla \cdot (\rho \mathbf{u}) = 0. \quad (1)$$

Conservation of linear momentum requires

$$\begin{aligned} \frac{\partial(\rho \mathbf{u})}{\partial t} + \nabla \cdot (\rho \mathbf{u} \mathbf{u}) &= -\nabla P + \nabla \cdot (\mu(\nabla \mathbf{u} + \nabla \mathbf{u}^T)) \\ &+ \Sigma \mathbf{f}_i + \mathbf{f}_{lv}^\sigma, \end{aligned} \quad (2)$$

where P is the pressure (Lagrange multiplier to enforce mass conservation for incompressible flows), \mathbf{f}^σ the surface tension force, and $\Sigma \mathbf{f}_i$ the summation of the external forces. The mixture physical properties are defined as $\rho = \rho_l \phi_l + \rho_v \phi_v + \rho_w \phi_w$ and $\mu = \mu_l \phi_l + \mu_v \phi_v + \beta \mu_l \phi_w$ (details concerning β will be discussed in subsequent sections). For constant bulk densities and in the absence of phase change, mass conservation can be re-expressed as

$$\nabla \cdot \mathbf{u} = 0, \quad (3a)$$

$$\frac{\partial \phi_l}{\partial t} + \nabla \cdot (\mathbf{u} \phi_l) = 0. \quad (3b)$$

Here I have made use of volume conservation $\phi_l + \phi_v + \phi_w = 1$ and considered the solid as a rigid body $\nabla \cdot (\mathbf{u} \phi_w) = 0$. To ensure a constant interface thickness, the following conservative equation is used:

$$\frac{\partial \phi_l}{\partial t^*} = \nabla \cdot \left(W^2 \mathbf{r}_{lv} - W \sqrt{2} \phi_l \phi_v \frac{\mathbf{r}_{lv}}{|\mathbf{r}_{lv}|} \right). \quad (4)$$

The details of the derivation of this equation and its numerical solution will be presented in the subsequent section.

III. SURFACE TENSION FORCE

The derivation of the surface tension force presented in the following is the main contribution of the present work. This force, which is nonzero only for curved interfaces, is commonly confused with the surface tension (or surface energy), which is a property of the interface independent of its curvature. From a microscopic mechanical point of view, surface tension arises from the loss of rotational symmetry of the capillary stress tensor inside the liquid-vapor interface [24]. The interpretation of an interface as a symmetry breaking of a tensor field is quite analogous to the idea of a particle in quantum physics. For high energy levels, let us say above the critical point, no symmetry breaking is observed and the liquid-vapor interface no longer exists. It is quite interesting to see that the same basic ideas from particle physics can be applied to much larger scales in a fractal-like fashion. From the definition of the capillary stress tensor presented in Ref. [24] [Eqs. (67) and (68)], it is simple to see that the tangential components of the stress tensor are lower than the normal one by the amount $\sigma_{nn} - \sigma_{tt} = \sigma_{nn} - \sigma_{ss} = \lambda_{PF} |\nabla \phi_l|^2$, which is the definition of the distributed surface tension and whose integral across the liquid-vapor interface correspond to the macroscopic value (measured experimentally). In the same work it was shown that the normal component of the stress tensor does not change across the interface but the tangential components do. This means that an element of fluid inside the liquid-vapor interface [see Fig. 2(b)] experiences lower tangential stresses than in the bulk phases, which places the fluid under tension in the tangential directions. These stresses are independent of the interface curvature, and therefore the fluid inside the interface is under tension (along the tangential directions), even for a flat interface. A tensile state along the tangential direction does not necessarily mean that molecules experience a net force pointing towards the liquid phase; in fact, the net force (known as surface tension force) is zero for a flat interface. For a bubble immersed in a liquid or a drop in a vapor, the surface tension force always points towards the confined phase. Hence, the pressure inside a bubble or a drop is always higher than the pressure in the surrounding fluid. For a system undergoing a phase transition, highly curved interfaces will have an important impact on the interface temperature. For instance, if we define a reference saturation temperature for a flat interface, then the interface temperature for a bubble or a drop will be higher and lower than that of the reference state, respectively. For drops, molecules located at the interface will have, on average, a lower number of neighboring molecules than in a bubble of the same size, which facilitates their evaporation. Therefore, drops or bubbles under local thermodynamic equilibrium will be subcooled or

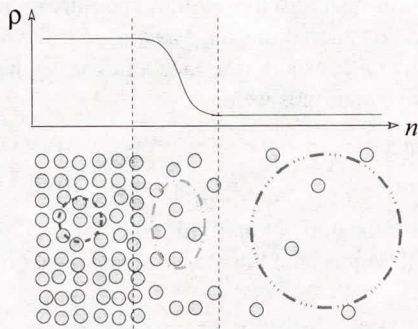


FIG. 1. (Color online) Schematic for the density profile across the liquid-vapor interface. The dashed blue and dash-dot-dotted red circles represent the isotropic mean distance between molecules in the bulk liquid and vapor, respectively. Inside the diffuse interface, the average distance between molecules in the tangential direction must be longer than that in the normal direction, which is exemplified by a dash-dotted green ellipse.

superheated respect to the reference state (a flat interface). An schematic of the density profile across the liquid-vapor interface is shown in Fig. 1, where the density is assumed constant in the bulk phases. If the normal vector is defined by the density gradient, then any variation of the density along the tangential directions is zero (the density is defined in terms of isodensity surfaces). The steep variation of the density along the normal direction, defined by its gradient, necessarily implies that the mean distance between molecules in the tangential directions is longer than that in the normal direction. Hence, the intermolecular interactions tangent to the interface are weaker, which translates into lower stresses. In the bulk vapor phase, the mean distance between molecules goes back to an isotropic behavior. Thus, the anisotropy of the stress tensor inside the liquid-vapor interface, and the existence of the surface tension, find an explanation in the anisotropic distribution of the mean distance between molecules. For two immiscible fluids with similar density, the interface can be described in terms of the local composition, and thus surface tension will arise due to the anisotropic strength distribution of the chemical bonds inside the interface.

From energetic considerations at a microscopic level [Fig. 2(a)], a contact angle can be explained as the geometrical response of the liquid-vapor interface, in the proximity of a third phase, to restore the same energy level as that of the interface far from the contact line. The micropotential energy of an atom (or molecule) in a liquid state is given by the strength and number of bonds with neighboring atoms (long- and short-range interactions). Atoms located at the liquid-vapor interface possess, on average, fewer atomic bonds than their counterparts in the bulk liquid phase. The fewer number of bonds translates into a higher energy level (potential energies associated to atomic interactions are negative), which facilitates their evaporation and surface diffusion. For a liquid atom located near the contact line, the interaction with the wall will change (increase or decrease) its micropotential energy, and, therefore, to re-establish it to the same level than that of an atom located at the liquid-vapor interface far from the contact line, the number of bonds with its neighboring liquid atoms must change. In the case of a droplet deposited on a flat surface,

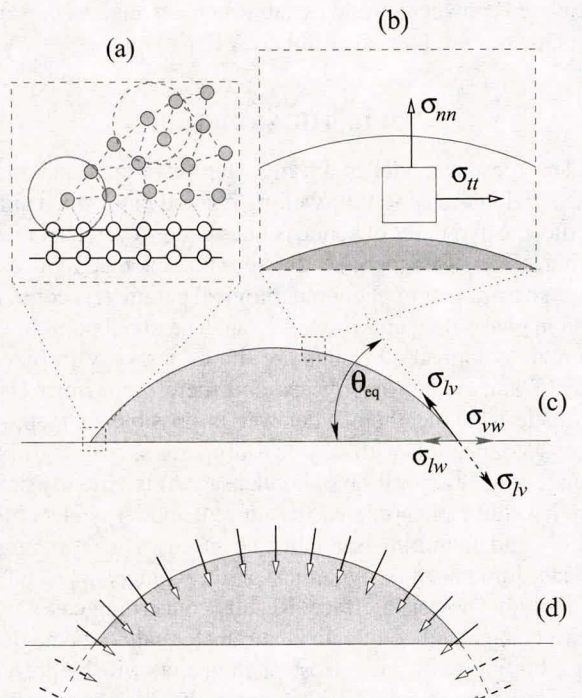


FIG. 2. (Color online) Schematic for wetting phenomena. (a) Molecular representation of the contact line, where interatomic interaction are depicted in dashed blue (liquid-liquid) and dash-dotted green (liquid-solid). The red circles represent the extent of short- and long-range interactions at the contact line (continuous) and at the “bulk” liquid-vapor interface (dashed). (b) Stresses inside the liquid-vapor interface. (c) Common representation of surface energies as forces at the contact line. (d) Surface tension force distribution along the liquid-vapor interface, extending into the solid wall (dashed arrows).

a lower strength between liquid-solid interaction necessarily implies a higher number of bonds between neighboring liquid molecules in the proximity of the contact line. Therefore, if the contact angle is measured between the tangent line of the liquid-vapor interface and horizontal line [Fig. 2(c)], weaker liquid-wall interactions translate into higher contact angles.

For a drop without the influence of gravity, its most favorable geometrical configuration is given by an spherical shape, which assures that, on average, each interfacial atom or molecule has the same number of bonds along a given isodensity surface. Despite that the spherical shape is the most favorable geometrical configuration, thermodynamic equilibrium is almost impossible to be achieved. A drop of water suspended in midair will slowly evaporate (or condense) depending on the moisture content of the air surrounding it. Since air is a mixture composed of several gases with different solubility in water, the dynamic behavior of our small drop is quite complex. If, for the sake of simplicity, we omit evaporation or condensation phenomena, an spherical shape can have a two-folded explanation: First, a sphere has the lowest surface-to-volume ratio. Second, the total curvature along its surface is constant, which translates into a constant pressure inside the drop. For a drop deposited on a flat surface, a minimization of the surface energy leads to the well-known

Young's equation $\sigma_{lv}\cos\theta_{eq} = \sigma_{vw} - \sigma_{lw}$, where θ_{eq} is the equilibrium contact angle and σ_{ij} are the surface energies (for a simple derivation of this equation the reader is referred to Ref. [27]). This equation is valid under the assumption that the solid surface is flat and that the liquid-solid energy is constant throughout the contact area. For rough surfaces, Wenzel [28], and then Cassie and Baxter [29], addressed the apparent contact angle based on the change of the contact area compared to the reference case of a flat surface. As pointed out by Gao and McCarthy [30], the equations proposed by Wenzel, Cassie, and Baxter reinforce the idea that the apparent contact angle does indeed depend on the contact area between the liquid and solid. Nonetheless, Gao and McCarthy not only questioned the work from Wenzel, Cassie, and Baxter, but they plainly stated that those theories are wrong. To validate their claim, they performed a series of experiments where islands of different chemical composition and topology were introduced on a flat silicon surface. Then they placed droplets with a contact area larger and smaller than the islands and measured the advancing a receding contact angles. They showed that the contact angles (advancing and receding) were independent of the modified surface as long as the contact area was larger than that of the modified island. They concluded that the contact angle behavior is solely dictated by interactions between the liquid and the solid in a zone very close to the contact line. The derivation of the surface tension presented in the following carries in it the idea that localized interactions at the contact line are the main responsible for a macroscopic contact angle, where the atoms or molecules located at the triple junction (contact line) are advected by a velocity field originated from a local unbalanced stress field.

Far from the contact line, the surface tension force is given by $\mathbf{f}^\sigma = -\nabla \cdot \vec{\sigma}_c = \hat{\mu} \nabla \phi_l$ (Eq. (74) in Ref. [24]), where $\vec{\sigma}_c$ is the capillary component of the stress tensor and $\hat{\mu}$ is a potential that controls the intensity of the surface tension force. If a liquid drop is deposited on a flat surface and is under mechanical equilibrium, the intensity of this force should be constant over the entire interface and point in the normal direction towards the liquid phase. This is also true at the contact line. In Fig. 2(d), the surface tension force is depicted with continuous arrows at the liquid-vapor interface and with dashed arrows in the projected interface into the wall. From conservation of momentum Eq. (2) we have that mechanical equilibrium is achieved if

$$-\nabla P + \mathbf{f}^\sigma + \Sigma \mathbf{f}_i = 0, \quad (5)$$

which is the differential form of the Young-Laplace equation. This equation must be satisfied over the entire system, including the liquid-vapor interface and the contact line. This condition for mechanical equilibrium differs radically from the one expressed by Young's equation, and that is because because Young's equation does not represent a condition for

mechanical equilibrium but rather a constraint to satisfy the minimization of the surface energy. The derivation of the surface tension force presented in the following aims to satisfy Eq. (5) even inside the contact line (three-phase region). We start the derivation from the free-energy functional for two-phase systems presented in Ref. [24],

$$\Pi_0 = \int_{\Omega} f(\phi_l, \phi_v, \nabla \phi_l) d\Omega, \quad (6)$$

where the free-energy density is defined as

$$f = -p_{eq}(T) + 16\Delta f_{max} \phi_l^2 \phi_v^2 + \frac{1}{2} \lambda_{PF} |\nabla \phi_l|^2. \quad (7)$$

The transformation potential for each phase is given by

$$\mu_i = \frac{\partial f}{\partial \phi_i} - \nabla \cdot \left(\frac{\partial f}{\partial \nabla \phi_i} \right), \quad (8)$$

and, thus, the transformation potential derived in Ref. [24] corresponds to the difference between the potential for the liquid and vapor $\hat{\mu} = \mu_l - \mu_v$. When we have a system composed of a binary fluid (e.g., liquid and vapor) and a solid wall, the volume conservation states that $\phi_f + \phi_w = 1$ and $\phi_l + \phi_v = \phi_f$, where the subindexes f, w, l , and v denote fluid, wall, liquid, and vapor. The second condition can be rewritten as $\phi_l^* + \phi_v^* = 1$, with $\phi_l^* = \phi_l/\phi_f$ and $\phi_v^* = \phi_v/\phi_f$. The normalization of the liquid and vapor volume fractions is required to describe the free-energy density of the liquid-vapor interface in the proximity of the wall, where the fluid fraction starts to be less than 1. The main idea is that even though the fluid fraction is decreasing as we move deeper into the solid phase, we will focus our attention only on the free energy of the fluid phase. Thus, to account for the presence of the wall in the free-energy density, we simply replace the standard phase fields with the normalized ones ($\phi_i \rightarrow \phi_i^*$). In addition, we allow the inhomogeneous coefficient to be dependent on the wall phase field ϕ_w [$\lambda_{PF} \rightarrow \lambda_{PF}(\phi_w)$]. With this, the free-energy functional reads

$$\begin{aligned} \Pi_1 = \int_{\Omega} & \left\{ -p_{eq}(T) + 16\Delta f_{max} \frac{\phi_l^2 \phi_v^2}{\phi_f^4} \right. \\ & \left. + \frac{1}{2} \lambda_{PF}(\phi_w) \frac{|\mathbf{r}_{lv}|^2}{\phi_f^4} \right\} d\Omega, \end{aligned} \quad (9)$$

where $\mathbf{r}_{lv} = \phi_v \nabla \phi_l - \phi_l \nabla \phi_v$. The same vector was proposed by Steinbach *et al.* [31] to account for the inhomogeneous free-energy density in their multi-phase-field formulation. This vector is easily derived by taking the gradient of the normalized liquid phase field and applying volume conservation (see Appendix A). Considering an inhomogeneous coefficient λ_{PF} independent of ϕ_l and ϕ_v , the transformation potential for the liquid-vapor interface reads

$$\hat{\mu} = -\frac{4\sigma}{WI_0} \left[\frac{W^2 \phi_f \nabla \cdot \mathbf{r}_{lv} - 2\phi_l \phi_v (\phi_v - \phi_l) + 2W^2 |\mathbf{r}_{lv}| |\nabla \phi_w| \cos(\theta) + (W/\sigma) \phi_f \mathbf{r}_{lv} \cdot \nabla (\sigma W)}{\phi_f^4} \right], \quad (10)$$

where σ is the surface tension, $W = \sqrt{\lambda_{PF}/16\Delta f_{max}}$ a measure of the interface thickness, and $I_0 = 2\sqrt{2}/3$ [24]. The last term

in Eq. (10) accounts for possible variations of the surface tension and interface thickness in the nearby region to the wall

(see Appendix B for a detailed derivation). At macroscales, these variations are negligible, but at microscales the interface properties could potentially suffer significant deviations from their bulk values, due to molecular interactions with the wall. A departure from bulk values could lead to important changes in the shape of the liquid-vapor interface in the proximity of the contact line. The angle θ formed between \mathbf{r}_{lv} and $\nabla\phi_w$ is an instantaneous quantity that changes in time, but by fixing it to the macroscopic equilibrium contact angle θ_{eq} , the system relaxes towards the desired configuration. In the present model, the equilibrium contact angle must be interpreted as a thermodynamic quantity that is the macroscopic representation of the atomic interactions at the contact line. As previously discussed, the contact angle can be understood as the response of the liquid-vapor interface to restore the energy level of molecules near the contact line to the same level as those molecules located at the interface far from it. By fixing the contact angle in Eq. (10), we are setting the desired energy level of the molecules at the contact line. It is important to note that the equilibrium contact angle introduced in the transformation potential will not necessarily be equal to the apparent contact angle, which is the result of a force balance at the contact line. For instance, a drop of water attached to an inclined plane will display a variation of the apparent contact angle along the contact line, but the wetting properties of the surface are independent of gravity and therefore the equilibrium contact angle remains unchanged. Replacing the rescaled volume fraction in the surface tension force, originally derived for two-phase flows [24], leads to the final expression,

$$\mathbf{f}_{lv}^\sigma = \hat{\mu} \frac{\mathbf{r}_{lv}}{\phi_f^2}. \quad (11)$$

This force reduces to the original expression derived in Ref. [24] for $\phi_f = 1$. Since this force was obtained using the normalized volume fractions, it extends well into the solid region. Nonetheless and since the velocity field is set to a null value for wall volume fractions higher than 0.5 ($\mathbf{u} = 0$ for $\phi_w > 0.5$), the intensity of the surface tension force inside the solid phase is irrelevant. The magnitude of this force depends on the local interface curvature (implicitly included in $\hat{\mu}$) and the difference between the apparent and equilibrium contact angles. Therefore, for configurations away from equilibrium, the intensity of the surface tension force will vary sharply at the contact line. This variation arises from an unbalanced stress tensor, in the same way Qian *et al.* [4] observed in their molecular dynamic simulations. Thus, under nonequilibrium conditions, the surface tension force promotes a slip between the fluid and the wall, allowing the contact line to move. The incompatibility of conventional hydrodynamics with the nonslip boundary condition at the contact line arises from the wrong interpretation of the stresses. The nonslip boundary condition exists because the shear stress at the wall is not able to overcome molecular interaction between the fluid and solid. Nonetheless, at the contact line there is an additional component to the stress field that causes the interface to move. Therefore, even if we set the velocity in the solid phase equal to 0, the fluid right above it will still experience an unbalanced stress field, resulting in the motion of the contact line towards a more favorable configuration. It is important to remark that in the present derivation of the surface tension force,

only the interface thickness W is a free parameter. The rest of the parameters are clearly defined and linked to physical properties. In the present work W is related to the grid spacing by $W = (1.3 \sim 1.5)\Delta x$, and it must be regarded as parameter that controls the rate of convergence of the present model towards the sharp interface limit.

IV. RESHARPENING EQUATION

Since the phase field associated to the wall does not change in time, we can solve the whole problem based only on the evolution of a single phase field, which in this case is the one associated to the liquid phase. The dynamic evolution of the vapor can be obtained by applying volume conservation, that is, $\partial_t \phi_v = -\partial_t \phi_l$. The evolution of the liquid phase field is governed by Eq. (3b). Hence, the phase field evolves only by virtue of the velocity field and not by diffusion, in contrast to hydrodynamics Cahn-Hilliard (CH) models where diffusion plays an important role. In CH models, the interface thickness is maintained by adding a diffusion current $\nabla \cdot (M \nabla \hat{\mu})$ to the right-hand side of the phase-field equation, where M is a positive constant. Nonetheless, there are some fundamental problems with that approach, which can be better understood with a simple example. Let us imagine a deformed air bubble immersed in water and analyze its evolution towards a hypothetical equilibrium state (perfect sphere). In hydrodynamic CH models, the bubble will evolve towards equilibrium by two parallel transport mechanisms: advection and diffusion. If the mobility coefficient M is too high, diffusion will dominate the path to equilibrium. Conversely, if the mobility is too small, advection will dominate the dynamics of the interface. The problem is that for small mobility coefficients, the interface will not keep its shape and deviations from the conventional hyperbolic tangent profiles will be important under strong advecting flows. Nonetheless, if a mobility coefficient is set to a value that is too high, important phenomena such as capillary waves (which are inherently controlled by advection and surface tension effects) will not be properly captured. For near atmospheric conditions, the dynamics of liquid-vapor interfaces should be mostly controlled by advection, and therefore any change of the interface morphology due to an artificial diffusion current is unphysical. In analogy to the Laplace number defined as $\mathbf{La} = \frac{\sigma L}{\rho v^2}$, where v is the kinematic viscosity and L is an arbitrary length scale, we can define a modified Laplace number to evaluate the relative importance of surface tension and diffusion. Thus this modified Laplace number is defined as $\mathbf{La}^* = \frac{\sigma}{\rho \kappa D^2}$, where κ is the local interface curvature and D the self-diffusion coefficient. For water at room temperature, these parameters are given by $\sigma = 0.072 \text{ N/m}$, $\rho_l = 1000 \text{ kg/m}^3$, and $D = 2.3 \times 10^{-9} \text{ m}^2/\text{s}$. Thus, the modified Laplace number is of the order of $\mathbf{La} \approx 10^9$ for a bubble with a radius of 1 mm, which indicates that diffusion does not play any role in the dynamics of liquid-vapor interfaces. Since the surface tension vanishes at the critical temperature and the diffusion coefficient increases exponentially with temperature, it is envisioned that for temperatures slightly below the critical temperature, diffusion might be the dominant mechanism. For phase separating systems, diffusion will play a fundamental role in the initial stages of the phase separation, but if the surface tension of

freshly formed interfaces is large (compared to the diffusion coefficient in terms of the modified Laplace number), then the interfaces will evolve mostly by capillary phenomena. The original CH equation was derived in the context of the spinodal decomposition, which is a phase change purely controlled by diffusion. Thus, the use of this type of equation must be reserved for processes where the CH physics applies, e.g., phase separation in the solid state or to phase separation in liquid systems with a small modified Laplace number. To avoid the unjustified use of the diffusion current to maintain the interface shape, the approach presented in Ref. [24] is used. In that work, it was shown that the transformation potential for two-phase systems can be split into two main parts: one controlling phase change and another controlling the interface shape. The part controlling the shape of the interface can be written in a conservative way, which leads to a resharpening equation that allows for maintaining the interface shape without modifying its curvature. A modified version of this equation is required to account for the wall. This is accomplished by replacing the normalized volume fraction of the liquid and vapor phases into the original resharpening equation presented in Ref. [24]. Thus, the resharpening equation reads

$$\frac{\partial \phi_l}{\partial t^*} = \phi_f \nabla \cdot \left(\frac{W^2 \mathbf{r}_{lv}}{\phi_f^2} - \frac{W\sqrt{2}\phi_l\phi_v}{\phi_f^2} \frac{\mathbf{r}_{lv}}{|\mathbf{r}_{lv}|} \right), \quad (12)$$

where t^* is a pseudo time step used to evolve ϕ_l to a profile that satisfies $W^2 \mathbf{r}_{lv} - W\sqrt{2}\phi_l\phi_v \frac{\mathbf{r}_{lv}}{|\mathbf{r}_{lv}|} = 0$. Since the dynamic evolution of this equation towards its solution is irrelevant, the same solution will be reached by solving

$$\frac{\partial \phi_l}{\partial t^*} = \nabla \cdot (W^2 \mathbf{r}_{lv} - W\sqrt{2}\phi_l\phi_v \mathbf{n}_{lv}), \quad (13)$$

where the normal vector is defined as $\mathbf{n}_{lv} = \frac{\mathbf{r}_{lv}}{|\mathbf{r}_{lv}|}$. Despite that the solutions of these two equations are equal, Eq. (13) is easier to solve numerically.

A. Numerical solution of the resharpening equation

Even though the resharpening equation appears to be simple in its form, its nonlinearity requires special care in the numerical solution. Being a conservative equation, it is quite natural to apply a finite-volume discretization to it. Figure 3 presents a conventional two-dimensional stencil for finite-volume discretizations. The flux at the east e interface is calculated by

$$J_e = W^2 \left(\phi_v^e \frac{\partial \phi_l}{\partial x} \Big|_e - \phi_l^e \frac{\partial \phi_v}{\partial x} \Big|_e \right) - \frac{W\sqrt{2}}{2} (\phi_l^P \phi_v^P \mathbf{n}_{lv}^P + \phi_l^E \phi_v^E \mathbf{n}_{lv}^E), \quad (14)$$

where $\phi_l^e = 0.5(\phi_l^P + \phi_l^E)$ and $\frac{\partial \phi_l}{\partial x} \Big|_e = \frac{\phi_l^E - \phi_l^P}{\Delta x}$. To determine the normal vector, an extended stencil was used for the calculation of $\nabla \phi_l$ and $\nabla \phi_v$ (see details in Ref. [32]). In that work, different schemes were proposed for the discretization of ϕ_l^e and $\phi_l \phi_v \mathbf{n}_{lv}$, but further calculations (not presented in here) showed that the scheme proposed in Eq. (14) is the most suitable for the present model.

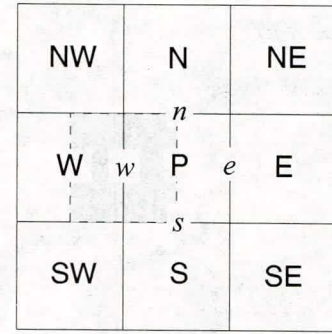


FIG. 3. (Color online) Finite-volume discretization in two dimensions. The colored control volume represents the staggered grid used for the calculation of the fluxes in the horizontal direction.

A pseudo time scale was chosen to be $dt^* = \alpha \sigma dt / W\sqrt{2}$, where dt is the physical time, σ the surface tension, and α a constant that only affects the convergence rate of Eq. (13). For a fully converged solution, the magnitude of α is irrelevant, but to optimize the computational resources, a good compromise between numerical stability and convergence rate must be sought. By trial and error, a value of $\alpha = 60 \frac{s \cdot m}{kg}$ was determined. The resharpening equation Eq. (13) was solved each time step until the change between two consecutive pseudo time steps was smaller than $\phi_l^1 - \phi_l^0 \leq 0.0001 \frac{\alpha \sigma dt}{\Delta x}$ or the number of iterations was higher than 5.

V. RESULTS: STATICS

All the simulations presented in the following (including those in the next section) were performed on high-performance computing facilities, using up to 2048 processors. The current model was implemented in our highly parallelized in-house code. More details on the code can be found elsewhere [33]. In all the simulations, the density of the wall was taken to be equal to that of the liquid; nonetheless, the simulations proved to be insensitive to this parameter for many solid materials.

A. Static contact angle

This is the simplest test for a model aiming to reproduce the physics of wetting. In this case, gravity was neglected. The physical properties of the fluids are $\rho_l = 1000 \text{ kg/m}^3$, $\rho_v = 1 \text{ kg/m}^3$, $\mu_l = \mu_v = 0.01 \text{ Pas}$ and $\sigma = 0.01 \text{ N/m}$. The interface thickness was set to $W = 1.5 \Delta x$ for all the simulations. By taking advantage of the symmetry of the problem, only one-fourth of the drops was simulated. The system size was $4 \times 4 \times 3 \text{ mm}$. The initial droplet radius was $R_0 = 1 \text{ mm}$ and a contact angle $\theta_0 = 90^\circ$. The numerical solution of the equations considered $96 \times 96 \times 72$ grid points and the time step was set to $dt = 5 \mu\text{s}$. Figure 4 presents the calculated static shapes of drops corresponding to five different equilibrium contact angles. To compare the phase-field simulations with analytical solutions (displayed in red dashed line), we must consider the normalized liquid phase field $\phi_l^* = \phi_l/\phi_f$ (displayed in blue dashed line). The phase field for the liquid phase ϕ_l does not properly represent the liquid-vapor interface at the contact line. The difference between ϕ_l^* and ϕ_l is most clearly seen for a contact angle equal to $\theta_{eq} = 30^\circ$. These results are

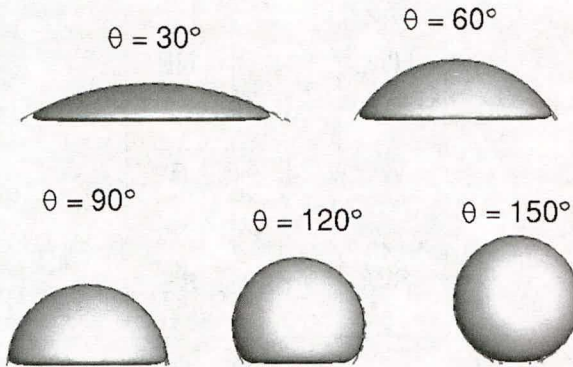


FIG. 4. (Color online) Tridimensional simulation of equilibrium configurations. The liquid volume is the same for the five cases. Dashed red lines correspond to the analytical solution given by the equilibrium contact angle. Surfaces correspond to $\phi_l = 0.5$ and continuous blue lines to $\phi_l/\phi_f = 0.5$ (normalized liquid phase field).

very accurate despite the coarse grid used in these simulations. Conventional phase-field models require much finer grids.

B. Wetting transition

To further assess the capabilities of the present model, I address the wetting transition on textured surfaces. The experimental work of Callies and Quéré [34] was used as a reference. As in their experiments, micropillars of $2 \mu\text{m}$ in diameter and $12 \mu\text{m}$ in height were generated on the solid surface. Using a square lattice for positioning the pillars, three levels of concentration of pillars were investigated ($\phi_s = 0.0097, 0.022, 0.087$), which correspond to separation distances of $d = 6, 12, 18 \mu\text{m}$. The fluids were water and air with physical properties $\rho_l = 1000 \text{ kg/m}^3$, $\rho_v = 1.25 \text{ kg/m}^3$, $\mu_l = 1.85 \times 10^{-5} \text{ Pas}$, $\mu_v = 0.001 \text{ Pas}$, and $\sigma = 0.072 \text{ N/m}$. The equilibrium contact angle was taken to be $\theta_{\text{eq}} = 110^\circ$. In their experiments, they considered a concentration of pillars $\phi_s \approx 0.01$, which translate into a separation distance of $d = 18 \mu\text{m}$. They found that above a critical radius of $R_c = 200 \mu\text{m}$, droplets were in a Cassie state. Below it, a Wenzel state was observed. They also pointed out the possible influence of the droplet size on the static configuration. To simulate the wetting transition and resolve the pillars with the computational mesh, droplets with sizes higher than the experimental critical value were not compatible with the available computational resources. A different route was taken whereby it was decided to increase the concentration of pillar and see if any transition is observed. The initial condition for the simulations considered a spherical cap with a liquid volume of $V = 9 \times 10^5 \mu\text{m}^3$ and contact angle of $\theta_0 = 60^\circ$ (see Fig. 5). This translates into a droplet base radius equal to $R_b = 97 \mu\text{m}$, which is below the experimental critical value. Hence, the static configuration of the droplet should be given by a Wenzel state. In agreement with the experiments, the present model predicts a Wenzel state [see Fig. 6(d)]. If we divide the experimental critical radius by the separation distance between pillars we have that $\chi_c = R_c/d = 11$. For the present simulations, this ratio takes the values of $\chi = R_b/d = 5.4, 8$, and 16.2 for $d = 18, 12, 6 \mu\text{m}$. The simulations also predict also a Wenzel state for a separation distance of

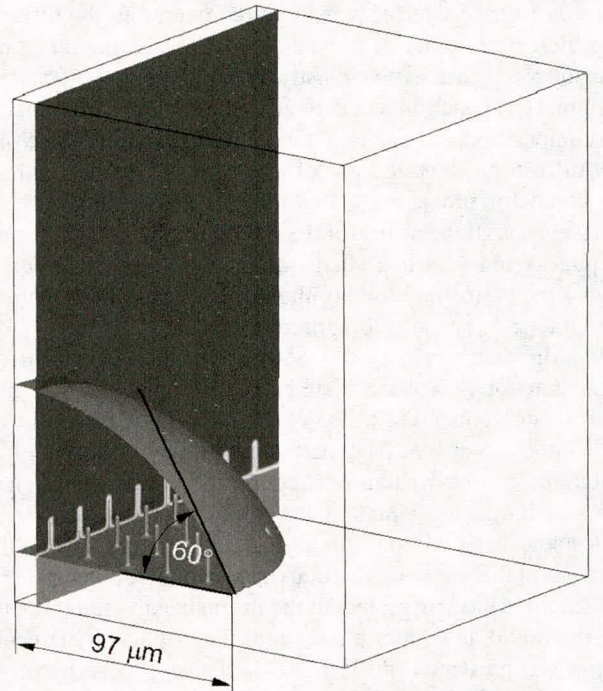


FIG. 5. (Color online) Initial condition for simulating the wetting transition. The droplet surface corresponds to a liquid phase field of $\phi_l = 0.5$. The wall phase field ϕ_w is displayed in colors.

$d = 12 \mu\text{m}$, but a Cassie state is found for $d = 6 \mu\text{m}$, which is the only case where $\chi > \chi_c$. These results suggest that what really matters in the wetting transition is not just the droplet size or the density of pillars but the combination of these two expressed in terms of χ . The arrangement of the pillars was also investigated. Figure 6(c) shows the results for randomly distributed pillars with the same concentration than that with separation distance $d = 12 \mu\text{m}$. From Fig. 6(b) and Fig. 6(c), it can be seen that the randomness in the pillar distribution does not have an effect on the configuration of the droplet. In fact, the difference between the maximum radius in these two

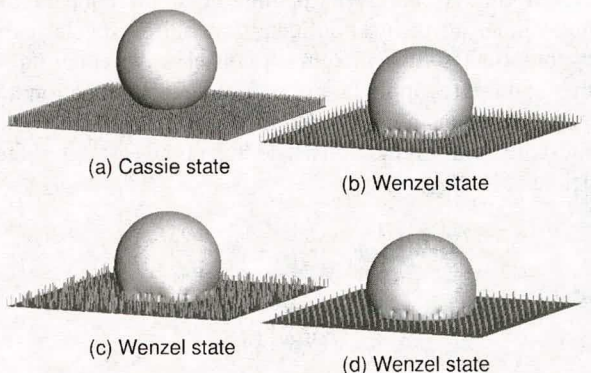


FIG. 6. (Color online) Wetting transition. This transition is realized by increasing the concentration of pillars in the surface for a constant liquid volume. Four cases were studied with separation distance between pillar of (a) $d = 6 \mu\text{m}$, (b) $d = 12 \mu\text{m}$, (c) $d = 12 \mu\text{m}$, and (d) $d = 18 \mu\text{m}$. In (c), the concentration of pillars is same as that in (b). The radius of the pillars is $1 \mu\text{m}$ and their height $12 \mu\text{m}$. For all the simulations $\beta = 7$ and $W = 1.3 \Delta x$.

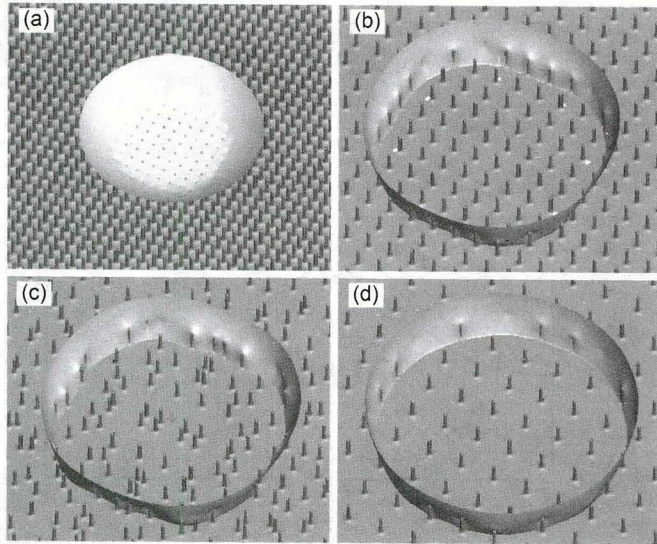


FIG. 7. (Color online) Details of the contact line for the final static configurations.

cases is less than 1%. Details of the contact line can be seen in Fig. 7. The Cassie state can be clearly appreciated in (a), where the liquid-vapor interface is only touching the tip of the pillars.

These results are initially counterintuitive, but they find a simple explanation. Consider a two-dimensional case as the one depicted in Fig. 8 with an equilibrium contact angle higher than 90° . When the contact line meets two pillars separated by a distance d , the surface tension force at the freshly formed contact line on the pillars (continuous green arrows) will try to form a contact angle close to that of equilibrium. As forces at the contact line between pillars (red and blue dashed arrows) push the contact line through the pillars, the intensity of the forces at the contact line on the pillars will increase to restore the proper contact angle. A static configuration is thus found when the integral of the surface tension force along the pillars compensates that from the contact line at the base. For a small separation distance between pillars, the contact line at the base must have a higher curvature to generate the same contact angle compared to a case with a larger separation distance. Since the surface tension force at the contact line depends on the local curvature and the deviation from the equilibrium contact angle,

a higher curvature means higher intensity, and, therefore, for a sufficiently small separation distance, the forces at the base contact line should overcome those coming from the pillars. For separation distances that are very large, the contact line at the base will dominate the wetting process. From these arguments, not only the separation distance between pillars but also the height of the pillars and their radius should have an effect on the static configuration. Nonetheless, the influence of these parameters was not investigated in the present work. The effect of the drop size also finds a simple explanation. The surface tension force in every point of the droplet surface depends on the total curvature, which is determined from the addition of two curvatures evaluated in two perpendicular directions (tangent to the surface). At the contact line, one curvature comes from the line itself and the second one from a perpendicular direction. In between pillars, only the second curvature is related to the droplet size. For a flat surface, these two curvatures are identical under equilibrium conditions and in the absence of body forces such as gravity. For the geometry and pillar distribution found in Ref. [34], the previous analysis indicates that a Wenzel state is the most favorable one for large droplets. Callies and Quéré showed in their experiments that it is possible to observe two droplets of the same volume in a Cassie and Wenzel state simultaneously on the same surface. This was achieved by “gently” pressing one of them to induce the Wenzel state. Nonetheless, they did not mention how “gently” the other droplet was deposited on the surface. By analyzing in more detail the morphology of the contact line for drops gently deposited or pressed onto the surface, it appears that the problem changes dramatically. For a drop gently deposited, the forces arising from the contact line at the pillars will have a completely different orientation than those in the case of a pressed droplet. Since the initial condition considered a spherical cap with a contact angle of $\theta_0 = 60^\circ$, the present simulations should be compared to experimental droplets that were gently pressed onto the surface (see Fig. 5). The effects of the droplet deposition will be left for a future study.

VI. RESULTS: DYNAMICS

A. Spreading drop

The first dynamic case addressed in this work is the spreading of a drop on a flat surface in the absence of gravity. Due to the symmetry of the problem, only one-half of the droplet was simulated. The simulation box was 4 mm in width and 3 mm in height. The initial condition considered a drop deposited on a flat surface with radius $R_0 = 0.7$ mm and initial contact angle of $\theta_0 = 156^\circ$. The grid was uniform with a spacing of $\Delta x = 41.7 \mu\text{m}$. To compare the present simulations with known results in the literature, the properties were chosen to match the cases simulated by Zahedi [35] and Sato and Niceno [36]. The properties for the base two-dimensional case are $\sigma = 0.0094 \text{ N/m}$, $\rho_l = \rho_v = 7.4 \text{ kg/m}^3$, and $\mu_l = \mu_v = 0.01 \text{ Pas}$.

Figure 9 presents a comparison for the dependence of the dynamic contact angle (see Appendix C for details of its numerical calculation) with the Capillary number $\mathbf{Ca} = U_{cl}\mu/\sigma$. Despite the fact that the current model produces

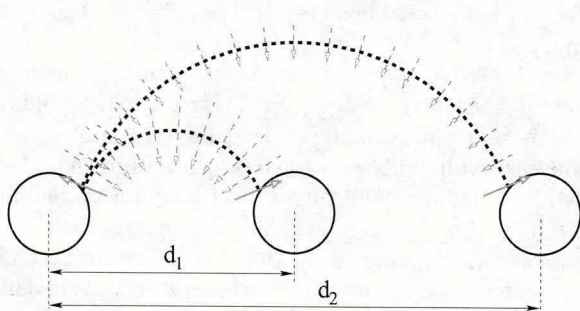


FIG. 8. (Color online) Schematic of the forces at the contact line on microstructured surfaces. The base contact line is depicted by a dashed black line. The contact line at the pillars is not visible, but its associated force is shown by continuous green arrows.

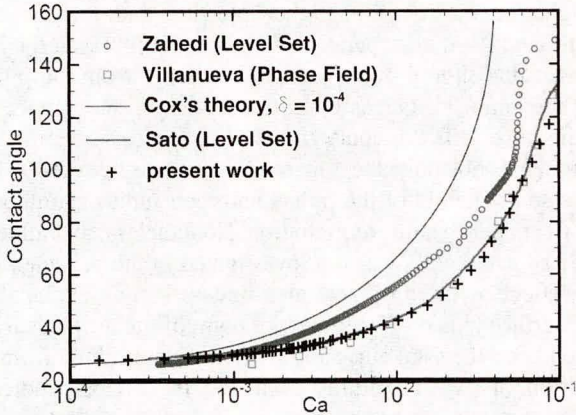


FIG. 9. (Color online) Dynamic contact angle (deg) against the capillary number.

results in very close agreement to those of Villanueva [37] and Sato [36] (finest grid), the relationship between the dynamic contact angle with the capillary number says nothing about the spreading rate. In fact, we can see from the dissipation rate Fig. 10 that the system has almost reached its static configuration after only 0.1 s in contrast to the time scales presented in Ref. [36].

In the same figure, the dissipation rate for several cases is presented. First, the base two-dimensional case (fluids with equal properties) is shown by the dashed green line, where it can be seen that after an initial adjustment of the system to its stable dynamic configuration (before 10 ms), the system enters a regime where the average dissipation rate changes its magnitude proportionally to $\langle \epsilon \rangle \propto t^{-2}$. Intriguingly, this scaling is in very close agreement with Kolmogorov's time scale. Indeed,

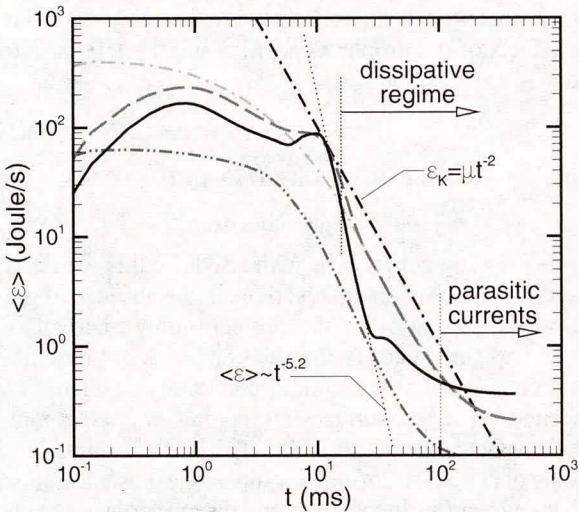


FIG. 10. (Color online) Volumetric averaged dissipation rate for a spreading drop $\langle \epsilon \rangle = \int \epsilon dV / \int dV$. Dash-dotted green: 2D, $\rho_l = \rho_v = 7.4 \text{ kg/m}^3$, $\mu_l = \mu_v = 0.01 \text{ Pas}$. Dash-dot-dotted red: 3D, $\rho_l = \rho_v = 7.4 \text{ kg/m}^3$, $\mu_l = \mu_v = 0.01 \text{ Pas}$. Dashed blue: 2D, $\rho_l = 1000 \text{ kg/m}^3$, $\rho_v = 1 \text{ kg/m}^3$, $\mu_l = \mu_v = 0.01 \text{ Pas}$. Continuous black: 2D, $\rho_l = 1000 \text{ kg/m}^3$, $\rho_v = 1 \text{ kg/m}^3$, $\mu_l = 0.01 \text{ Pas}$, $\mu_v = 0.0001 \text{ Pas}$. The time step used in the simulations was $dt = 1.4 \mu\text{s}$ and $\beta = 1$.

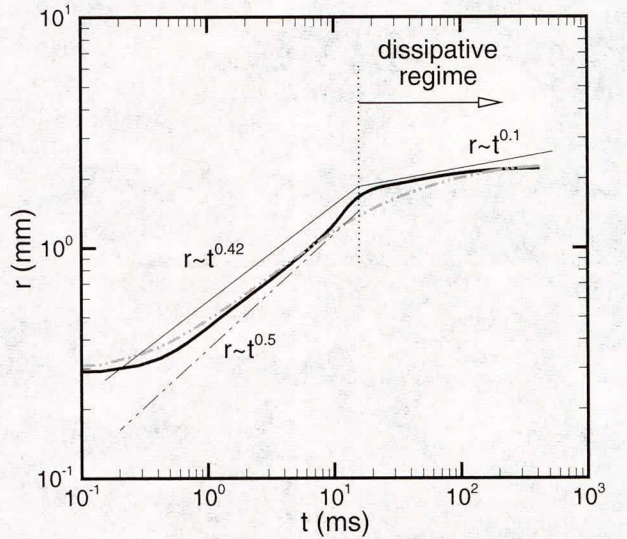


FIG. 11. (Color online) Radial position of the contact line against time. Dash-dot-dotted green: 2D, $\rho_l = \rho_v = 7.4 \text{ kg/m}^3$, $\mu_l = \mu_v = 0.01 \text{ Pas}$. Continuous black line: 2D, $\rho_l = 1000 \text{ kg/m}^3$, $\rho_v = 1 \text{ kg/m}^3$, $\mu_l = 0.01 \text{ Pas}$, $\mu_v = 0.0001 \text{ Pas}$.

when plotting μt^{-2} on the same plot, the agreement is evident. This scaling is also found in the three-dimensional simulation of the same case (red dashed line). Changing the densities to $\rho_l = 1000 \text{ kg/m}^3$ and $\rho_v = 1 \text{ kg/m}^3$ (blue dashed line) only affects the initial stages of the spreading, but it does not change the scaling of what appears to be a purely dissipative regime. Compared to the base two-dimensional (2D) case, this simulation only differs by its inertia. Hence, an inertial regime is identified at the early stages of the spreading, followed by a dissipation controlled regime. A quite different behavior is observed for high density and viscosity ratios $\rho_l/\rho_v = 1000$ and $\mu_l/\mu_v = 100$. In this case, the transition from the inertial to the dissipation regime occurs at a similar time, but the scaling for the dissipation rate differs substantially from the previous cases $\langle \epsilon \rangle \propto t^{-5.2}$. Close to the equilibrium configuration, the dissipation stops its decay and reaches a plateau due to the existence of low-intensity parasitic currents. Quéré and coworkers [38] also observed experimentally two distinctive regimes during the spreading of a drop of water brought in contact with a glass surface. They found that at the early stages of the spreading, the radius of the liquid in contact with the surface varied proportionally to $r(t) \propto t^{0.52 \pm 0.05}$. This scaling changed to $r(t) \propto t^{0.1}$, after what they identified as an inertial regime. These two exponents are in excellent agreement with the simulation with high density and viscosity ratios. Figure 11 shows the dynamic evolution of the radius of the liquid contact for the case with fluids with equal properties (green dash-dot-dotted line) and for fluids with high property contrast (continuous black line). For the case with high property contrast, the two exponents determined by Quéré *et al.* are in very close agreement with the simulation, where a very well defined transition is seen between the two regimes. These authors even obtained a characteristic time (Eq. (4) in Ref. [38]) where the inertial regime should end. This time is determined to be $\tau = 10.2 \text{ ms}$ for the simulation with high property contrast, which is almost in perfect agreement with the time at

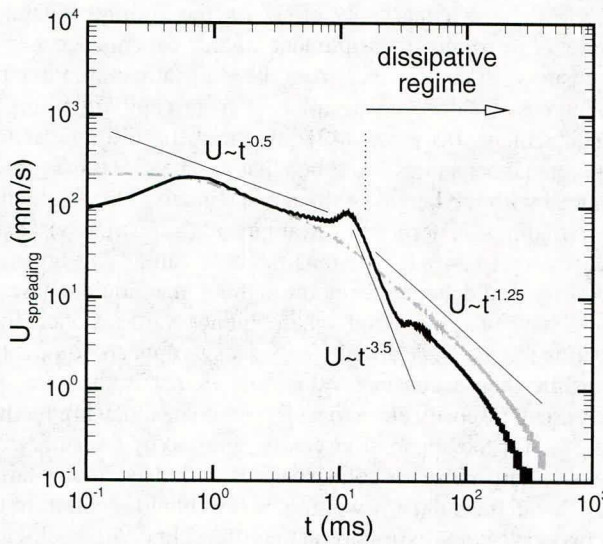


FIG. 12. (Color online) Spreading velocity against time. Dash-dotted green line: 2D, $\rho_l = \rho_v = 7.4 \text{ kg/m}^3$, $\mu_l = \mu_v = 0.01 \text{ Pas}$. Black line: 2D, $\rho_l = 1000 \text{ kg/m}^3$, $\rho_v = 1 \text{ kg/m}^3$, $\mu_l = 0.01 \text{ Pas}$, $\mu_v = 0.0001 \text{ Pas}$.

which the transition occurs in Fig. 11. The spreading velocity is presented in Fig. 12, where evidence for different scaling laws can also be seen. For the inertial controlled regime, the spreading velocity scales as $U_{\text{spreading}} \propto t^{-0.5}$, in agreement with the work of Wheeler *et al.* on the early stages of reactive wetting.

The fact that only the simulation with high property contrast is close to the experimental observations is quite encouraging, because this calculation is the closest to a real system. Nevertheless, the results from the simulation with fluids with no property contrast are quite interesting as well. The reasons for the good agreement between the scaling predicted by Kolmogorov's time scale and the present simulations are not totally clear. Nonetheless, a bold explanation is as follows. Kolmogorov's time scale represents the time required to quickly convert the kinetic energy, associated to the ordered collective mode of motion of molecules, into molecular disordered kinetic energy (heat). He postulated that in a turbulent flow, there is a length scale below which the dissipation rate is constant and equal to ϵ_0 . If this is true, then using dimensional arguments we arrive to the conclusion that there is a constant time scale, given by $\tau_0 = (\mu/\epsilon_0)^{1/2}$. If this time scale is correct, then it should apply to all the processes controlled by dissipation. If we express the dissipation rate and time in units of ϵ_0 and τ_0 , we have that in the dissipation controlled regime $\langle \epsilon \rangle t^2 = \epsilon_0 \tau_0^2 \times C$. From the present simulations the constant C is approximately $C = 2\mu$ and $C = 15\mu$ for 2D and 3D, respectively.

Since in the dissipative regime the density does not play any role, having a viscosity ratio equal to 1 is analogous to having a single-phase flow, with a momentum source term located at the liquid-vapor interface (surface tension force). Kolmogorov's time scale is only valid for single-phase flows, and thus, it can be expected that his scaling for the dissipation rate agrees well with the simulations with equal viscosities. For two-phase flows and close to the interfaces, such microscopic

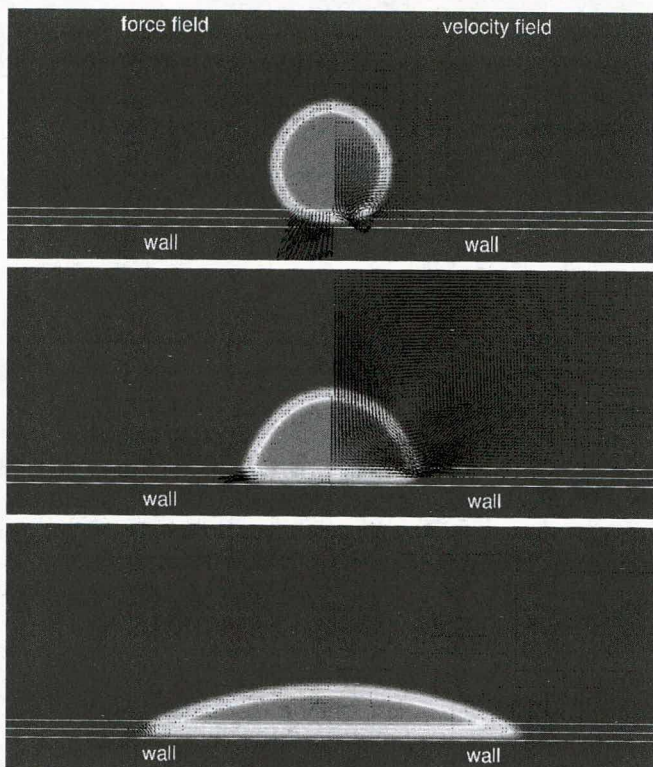


FIG. 13. (Color online) Sequence for the spreading of a two-dimensional drop. This simulation correspond to fluids with identical properties. The surface tension force is plotted on the left and the velocity field on the right. Note the inversion in the direction of the surface tension force at the contact line. White lines correspond to the wall phase field $\phi_w = 0.1, 0.5, 0.9$. Images are taken at time steps 1.4 μs , 7 ms, and 420 ms.

time scales have not yet been identified. The simulation with the high viscosity ratio confirms that the dissipative processes in two-phase flows follow a completely different scaling law than that of single-phase flows.

Figure 13 shows the force and velocity field during the spreading of a drop for fluids with equal properties. At the initial stages of the spreading, the surface tension force is very strong at the contact line and points in the opposite direction of the normal of the liquid-vapor interface (in contrast to the orientation of the force away from the wall). This strong force generates a slip velocity distribution at the contact line and the nearby regions (see Fig. 14), in agreement with the molecular dynamics simulations from Qian *et al.* [5].

B. Drop sliding

The next case under study is the dynamics of a drop sliding down an inclined surface. Here the experimental work of Le Grand and coworkers [39] was used to assess the quantitative capabilities of the current model. The parameters for the simulations are $\rho_l = 964 \text{ kg/m}^3$, $\rho_v = 1.25 \text{ kg/m}^3$, $\mu_l = 0.01 \text{ Pas}$, and $\mu_v = 18.5 \mu\text{Pas}$. A simple drop sliding down an inclined plane is one of the most difficult tests for any quantitative wetting model. The results of Le Grand *et al.* have been previously used by Koh [40] and Huang [41] to validate their models and good agreement with experimental data was

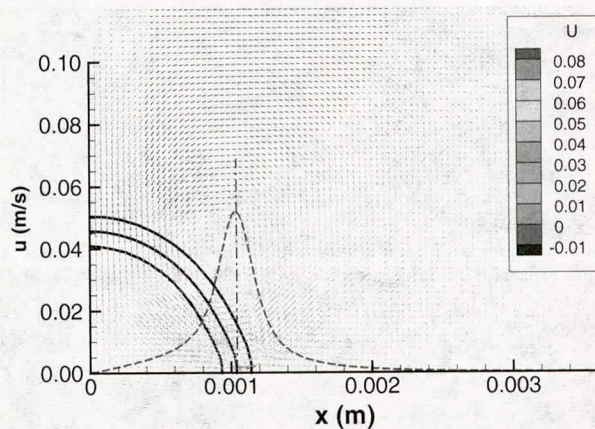


FIG. 14. (Color online) Slip velocity during the spreading of a drop on a flat surface at $t = 7$ ms. The results correspond to the base 2D case for the spreading drop with $\beta = 1$. The dashed red continuous line represents the slip velocity at the first cell above $\phi_w = 0.5$. Black continuous lines are the normalized liquid phase field at $\phi^* = 0.1, 0.5, 0.9$

found. Nonetheless, these authors simulated only the case corresponding to the lowest liquid viscosity. To the best of my knowledge, no results for the intermediate and highest viscosity have ever been reported. Le Grand and coworkers varied the viscosity of the droplets by changing their degree of polymerization, but no modification was made to the surface. They presented results for sliding velocities as a function of the inclination angle (**Ca** versus Bo_α) and found that the curves corresponding to the three completely different liquid viscosities do not collapse into a single master curve. They attributed this effect to small changes in the wetting properties, characterized by a slight variation of the equilibrium contact angle. By looking at their results in detail, it is difficult to conclude that the contact angle is only responsible for avoiding the collapse of the experimental data into one curve. The contact angle difference for the experiments corresponding to viscosities of 10 cP and 104 cP is only $\Delta\theta_{\text{eq}} = 2^\circ$. This difference increases to $\Delta\theta_{\text{eq}} = 5^\circ$ for 104 cP and 1040 cP. Even though the largest deviation for the equilibrium contact angle is found for intermediate and the highest viscosities, their proximity in the **Ca** versus Bo_α plot is better than that for the low and intermediate viscosities. In this work, numerical simulations for the low and intermediate viscosities prove, indeed, that the results for two quite distinctive viscosities collapse into a single curve when using the same equilibrium contact angle.

The second free parameter that enters the model is β (used in the calculation of the mixture viscosity $\mu = \mu_l\phi_l + \mu_v\phi_v + \beta\mu_l\phi_w$). This parameter influences the viscous stresses in a region very close to the wall surface. For $\beta = 1$, the viscosity of the liquid phase close the wall equals that of the bulk, but the viscosity of the vapor phase increases from its bulk value to that of the bulk liquid. Since the interface thickness of the phase field representing the wall is small, the vapor viscosity adjusts to its bulk value only after few computational cells from $\phi_w = 0.5$. Despite that the mass of fluid within the fluid-wall interface is negligible compared to the total mass of fluid, changing this parameter from 1

to 7 will have a markedly effect on the sliding dynamics. There is no direct measurement of the dependence of the viscosity with the distance from the wall (at nanoscales), but its increased value can be inferred from capillary filling in nanochannels. Tas *et al.* [42] measured the filling speed of water in nanochannels and found that the speed was drastically reduced with the height of the nanochannels. They explained their findings in terms of an augmented apparent viscosity that was up to 24% higher than the bulk value. This apparent viscosity could be uniform throughout the liquid phase or could have a distribution where higher values concentrate towards the walls. A distributed viscosity appears to be more plausible than a constant value, and if that is the case, the increase in viscosity close to walls should be much higher than the 24% for the apparent viscosity reported by the authors. If the viscosity close to solid surfaces is indeed much larger than that in the bulk, any wetting model should account for the increased viscous dissipation at the contact line. A β coefficient higher than 1 increases substantially the local dissipation at a region very close to the contact line, where the highest slip velocity is found. Away from the contact line, the slip velocity is several orders of magnitude lower than the peak value at the contact line. This can be seen in Fig. 14, where the distribution of the slip velocity for a spreading drop is displayed in a dashed red line (simulations correspond to the 2D base case of the spreading drop). From this velocity distribution, it is clear that the derivative of the velocity along the x coordinate can contribute considerably to the dissipation rate near the contact line. Taking $\beta = 1$ for simulating the experimental sliding drop for an inclination angle equal to $\alpha = 40^\circ$, resulted in sliding velocities 3 times higher than those measured by Le Grand and coworkers. Sliding velocities close to those from the experiments can be reached by increasing β to values in between 7 and 10 (see Fig. 17). Although an increased viscosity close to the wall might be physical, as discussed previously, a value of $\beta = 7$ results in a mixture viscosity 4 times larger than that of the bulk liquid at $\phi_w = 0.5$, which is unlikely to occur in reality. Nevertheless, a large β value might have more than a single physical interpretation, as will be seen in the following.

1. Surface roughness effects

To the best of my knowledge, quantitative simulations assessing the effects of surface roughness on the sliding velocity of a drop have not been reported. In the present work, an attempt is made to answer some of the questions related to this difficult topic. To quantify the effects of the surface roughness, three simulations for the same inclination angle of $\alpha = 40^\circ$ were performed on a flat and rough surface with a random distribution of pillars of $100 \mu\text{m}$ in diameter and $120 \mu\text{m}$ in height. The simulation domain consisted of a box with 3 mm in height and width and 12 mm in length. The grid spacing was $\Delta x = 46.9 \mu\text{m}$ and the time step $dt = 10 \mu\text{s}$. A symmetry boundary condition was applied at the symmetry plane of the problem to decrease the computational time. As can be deducted from the grid spacing and the geometry of the pillars, the mesh is too coarse to fully resolve all of the details of the rough surface. Nonetheless, the present simulation is only intended to show how a change in the surface morphology changes the sliding velocity but not to provide a detailed

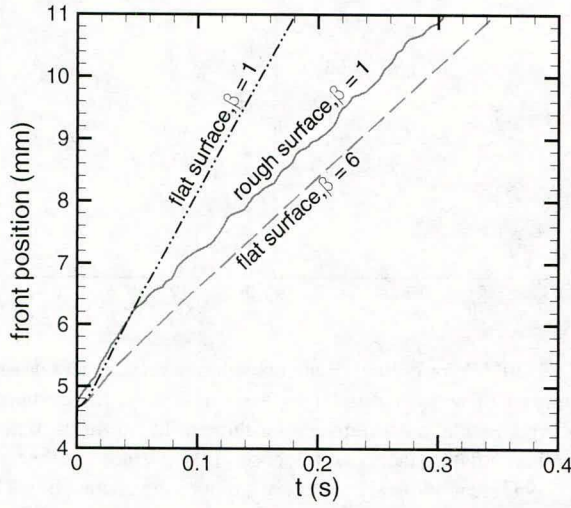


FIG. 15. (Color online) Front position for a sliding drop. Dash-dot-dotted black line: Flat surface with $\beta = 1$. Continuous red line: Rough surface with $\beta = 1$. Dashed blue line: Flat surface with $\beta = 6$.

quantitative description of the real surface roughness found in the experiments. The disparities of length scales are beyond the computational power at my disposal. The time evolution of the front position for three simulations is presented in Fig. 15. It can be seen that the front position advances at a similar speed for the flat and rough cases at the initial stages for $\beta = 1$. Nonetheless, after a short period, the front advances at a much lower speed on the rough surface. This lower sliding speed is related to the pinning effect of the micropillar in the same way observed in the wetting transition. Hence, on a rough surface, the direction and intensity of the surface tension force at the contact line differs markedly from that on a flat surface. By increasing the coefficient to $\beta = 6$ on a flat surface, a similar sliding velocity to that found with $\beta = 1$ on a rough surface is observed. The steady-state morphology of the droplets is presented in Fig. 16. It is seen that for achieving similar shapes, the sliding velocity must also be similar. The droplet on a flat surface sliding with $\beta = 1$ presents a more rounded shape compared to the other two cases, and that is because the wall exerts a lower resistance to its movement. If there is no resistance at all, the droplet base should be a perfect circle. The details of the surface roughness on Le Grand's experiment

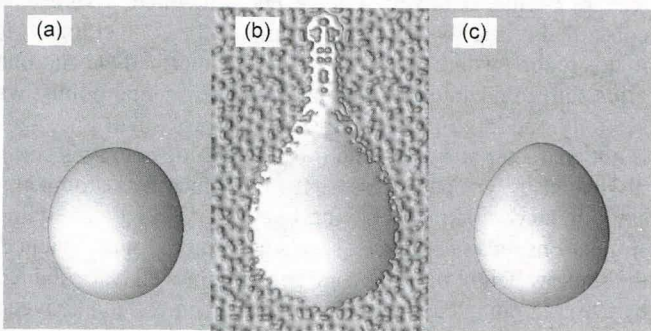


FIG. 16. (Color online) Steady-state morphology of sliding droplets. (a) $\beta = 1$; (b) $\beta = 1$; (c) $\beta = 6$. The surface of the droplets corresponds to $\phi_l = 0.5$.

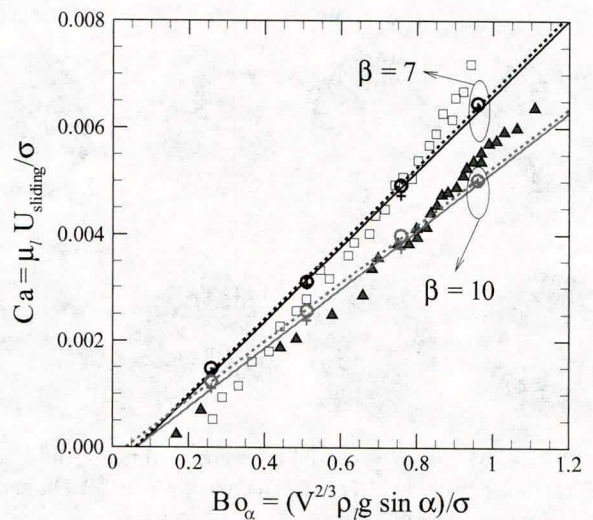


FIG. 17. (Color online) Capillary number versus the modified Bond number. Continuous lines represent the simulations for $\mu_l = 10 \text{ cP}$ and dashed lines for $\mu_l = 104 \text{ cP}$. Symbols are the experimental results digitized from Ref. [39].

were not presented in his paper. The present simulations show that by varying β , we can effectively capture the influence of the surface roughness on the contact line dynamics. At mesoscales and under dynamic conditions, this coefficient can be understood as a phenomenological parameter that reproduces simultaneously the effects of an increased viscosity close to the wall surface and the augmented forces at the contact line arising on rough surfaces.

2. Sliding on a flat surface

To further assess the model and the influence of β , several simulations were performed and directly compared to the experiments. For these simulations a domain twice as long as the previous one was used, with a grid spacing equal to $\Delta x = 32.25 \mu\text{m}$. Figure 17 presents the comparison between the calculated sliding velocity and the experimental values for four inclination angles. The lines represent linear interpolations of the numerical results. The continuous lines correspond to a viscosity of $\mu_l = 10 \text{ cP}$ and the dashed ones to $\mu_l = 104 \text{ cP}$. These results confirm that when plotting the sliding velocity and surface inclination in dimensionless form, through \mathbf{Ca} and \mathbf{Bo}_α , the simulations from two very different viscosities collapse onto a single curve. In all the simulations, the equilibrium contact angle was $\theta_{eq} = 50^\circ$. The effects of slight variations in this parameters is left for future studies. While increasing β decreases the slope of the curves, the critical inclination angle for the onset of motion is virtually unaffected. The critical $\mathbf{Bo}_\alpha = 0.07$ is estimated by a linear extrapolation of the numerical results. This value is roughly 1/3 of the measured one. Since β only affects the local energy dissipation at the contact line, it is evident that its influence on the critical Bond number is nonexistent. A more accurate calculation of the critical inclination angle is thought to be possible by including the details of the real surface roughness into the simulations, but this would be very computationally expensive. More details about the influence of

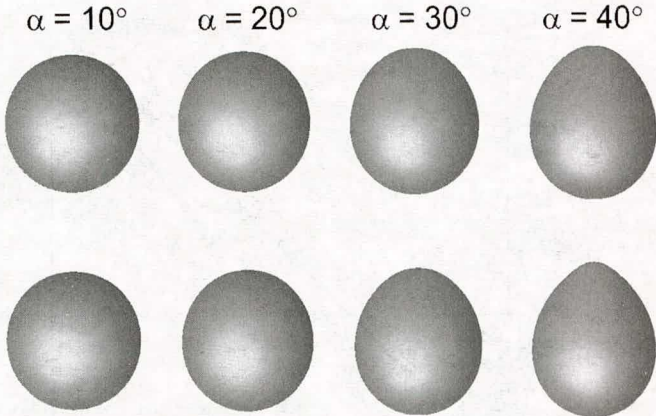


FIG. 18. Morphology of sliding drops at different inclination angles. First row: $\mu_l = 104$ cP, second row: $\mu_l = 10$ cP. The surface of the droplets correspond to $\phi_l = 0.5$.

the surface roughness on the contact line dynamics will be seen in the next case. Steady-state droplets at different inclinations and viscosities are shown in Fig. 18. The collapse of the calculated capillary number versus modified Bond number finds an explanation in the self-similarity in the droplets shapes. The experimental results from Le Grand present a quite unique opportunity to test any wetting model for predicting the self-similarity of sliding droplets.

For higher inclination angles, the simulations predict a pearling state, in agreement with the experiments. Figure 19 presents snapshots of the evolution of a droplet sliding on a plane with an inclination of 60° . A large disparity in the sliding velocity can be observed between the main droplet and the small ones shed in the wake. In the fourth image from left to right, three small droplets appear to have nucleated, but since the surface is represented by $\phi_l = 0.5$, these droplets were not visible before because at the moment they were shed, their associated liquid phase field was lower than 0.5. After a few instants, the droplets adopt their stable shapes.

C. Drop impact on a flat solid wall

The final case analyzed in the present work addresses the highly dynamic motion of the contact line during droplet impact on a solid surface. Yokoi *et al.* [43] measured the dynamic contact angle and the base diameter of a droplet of water during

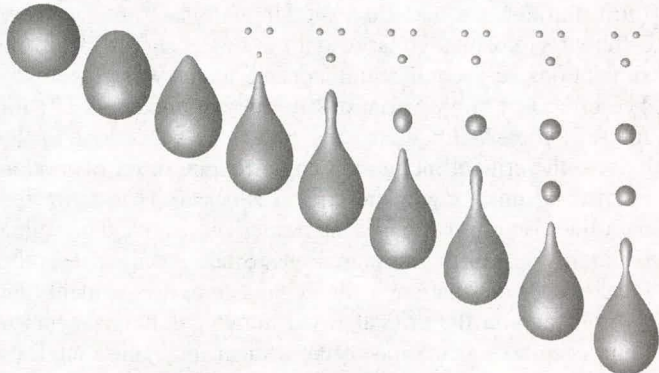


FIG. 19. Sliding droplet on a pearling regime for an inclination angle of 60° . Surface represented by $\phi_l = 0.5$.

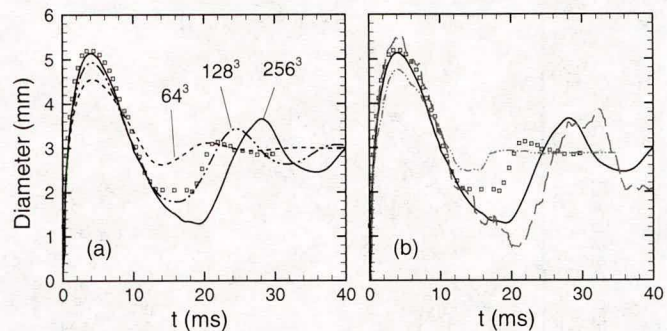


FIG. 20. (Color online) Radial position of the contact line during the impact of a water droplet on a solid surface. (a) Comparison with experimental measurements for three different mesh sizes with $\beta = 60$ on a flat surface. (b) Influence of the surface roughness and the β coefficient on the dynamic evolution of the contact line. Dash-dot-dotted blue line: $\beta = 60$ with pillars $78.2 \mu\text{m}$ in height. Dashed red line: $\beta = 1$ with pillars $125 \mu\text{m}$ in height.

the impact on a solid surface and used the experimental results to develop several models for the dynamic contact angle, which were then fed into a coupled level-set and volume-of-fluid simulation as a boundary condition. For one of the models, they found a very close agreement between the measured and predicted droplet base diameter and morphology. In the present work, no special models are required for the dynamic contact angle, which avoids the need for its experimental measurement. As is usual in this type of experiment, no detailed characterization of the surface roughness was presented. The present simulations considered only one-fourth of the droplet (due to the symmetry of the problem) and a computational volume of $4 \times 4 \times 4 \text{ mm}^3$. The volume was discretized with a grid spacing of $\Delta x = 62.4, 31.1, 15.6 \mu\text{m}$ for the coarse, intermediate, and fine grids, respectively. The time step was $dt = 1 \mu\text{s}$ for the coarse and intermediate grids and $dt = 0.5 \mu\text{s}$ for the finest one. The physical properties are $\rho_l = 1000 \text{ kg/m}^3$, $\rho_v = 1.25 \text{ kg/m}^3$, $\mu_l = 0.001 \text{ Pas}$, and $\mu_v = 18.2 \mu\text{Pas}$.

As expected for this highly dynamic case, $\beta = 1$ produces a spreading dynamics that is faster than those predicted by the experiments. To properly capture the spreading and recoiling rates, a coefficient $\beta = 60$ was used. Figure 20(a) shows the comparison between computed and experimental values of the droplet base radius for three different mesh sizes. Convergence can be clearly seen for the spreading and first recoil after impact (before 14 ms). Afterward comes a period which, I believe, is controlled primarily by pinning events at the contact line. It is in this regime where the results from the intermediate and fine grids start to deviate. Looking at the experimental points, we see only one large peak, followed by a very small one. This is not characteristic of a system whose kinetic energy is being dissipated by viscous stresses. If the surface was atomically smooth, an oscillatory behavior, like the one predicted by the simulations on a flat surface, seems to be more logical. Hence, the shallow height of the second peak might well be explained by a highly pinned contact line. A visual comparison between simulations (three mesh sizes) and experiments is presented in Fig. 21.

To assess the effects of the pinning events at the contact line, three simulations with a surface roughness represented by a

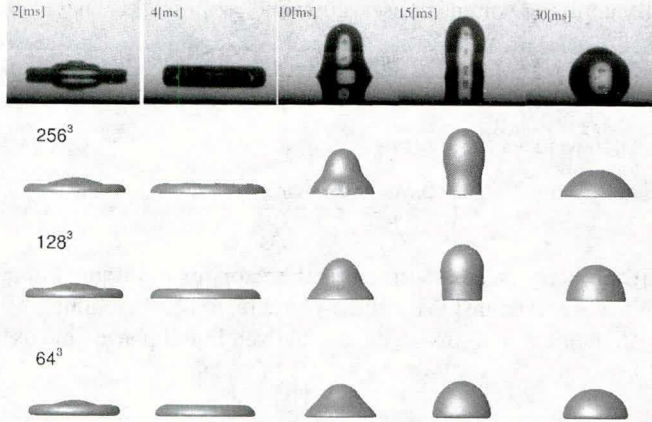


FIG. 21. Visual comparison between simulations (three mesh sizes) and experiments during droplet impact on a solid wall. Experimental images were taken from Ref. [43]. The surfaces correspond to $\phi_l = 0.5$.

random distribution of pillars, were performed. In Fig. 20(b) the evolution of the base radius for a flat surface with $\beta = 60$ is shown by a continuous black line. In red dashed line is the simulation with $\beta = 1$ and surface roughness given by pillars that are $125 \mu\text{m}$ in height and $50 \mu\text{m}$ in diameter and with a concentration of $\phi_s = 0.022$ (defined as the ratio of surface occupied by the pillars to the total surface). The latter captures the dynamics of the contact line almost in the same way as the simulation on a flat surface with $\beta = 60$, reinforcing the idea that $\beta > 1$ can indeed reproduce, on average, the major effects of pinning events during the motion of the contact line. For a static pinned contact line, β has no influence on the results. In the same figure, the dash-dot-dotted blue line corresponds to a simulation with same concentration of pillar and $\beta = 60$ but with slightly shorter pillars ($78.2 \mu\text{m}$ in height). The results show that a combination of high β and surface roughness can produce a contact line pinning stronger than the one observed

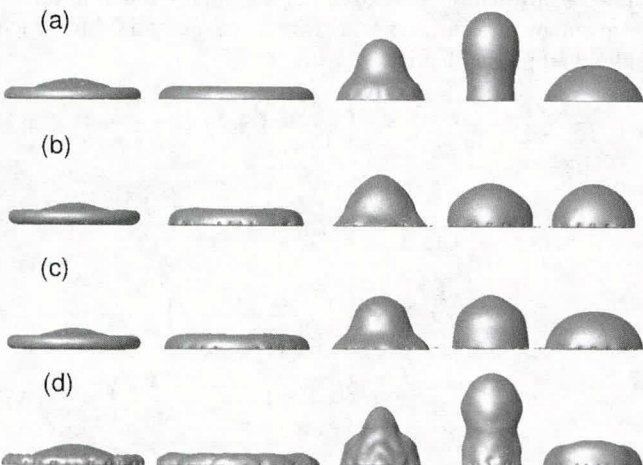


FIG. 22. Influence of β and surface roughness on the dynamics of the contact line and drop morphology. (a) Flat surface with $\beta = 60$. (b) Rough surface with $\phi_s = 0.022$, pillars height $125 \mu\text{m}$ and $\beta = 60$. (c) Rough surface with $\phi_s = 0.022$, pillar height of $78.2 \mu\text{m}$, and $\beta = 60$. (d) Rough surface with $\phi_s = 0.022$, pillar height of $125 \mu\text{m}$, and $\beta = 1$.

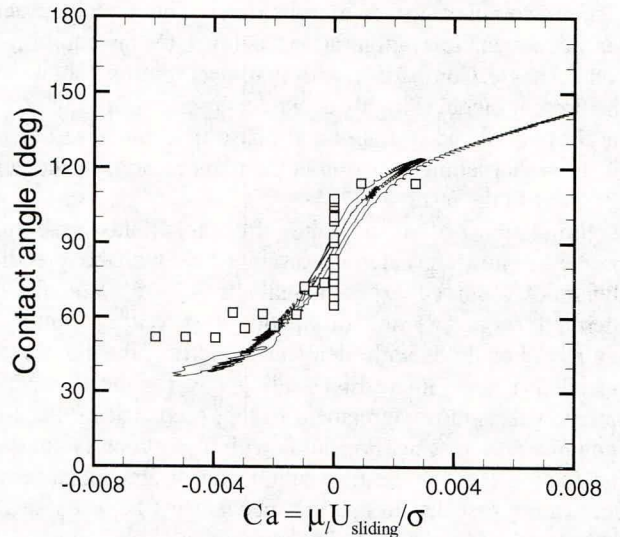


FIG. 23. Dynamic contact angle during droplet impact on a flat surface. The experimental results (symbols) were digitized from Ref. [43].

in the experiments. In the last simulation, not included in Fig. 20(b), the same β value was used, but the height of the pillars was increased back to $125 \mu\text{m}$. The pinning of the contact line was even stronger than in the previous case. The results for this simulation were not included in the plot, because a small droplet was shed during the spreading regime and the algorithm for tracking the contact line was only able to detect the small drop. Nevertheless, snapshots of the dynamic evolution for the four simulations can be seen in Fig. 22.

Aside from the capillary waves observed on Fig. 22(d), the overall dynamic evolution is very similar for cases (a) and (d) [also seen in Fig. 20(b)]. The influence of the pillars' height is appreciated in Figs. 22(b) and 22(c), where higher pillars produce stronger pinning events at the last stages of the whole process. Finally, a comparison between the calculated and experimental dynamic contact angle is presented in Fig. 23. The results show a clear hysteresis of the dynamic contact angle with the capillary number, revealing that, indeed, there is no universal function to correlate θ_d with \mathbf{Ca} . The angle hysteresis is the largest at $\mathbf{Ca} = 0$, where its value varies between 80° and 95° .

VII. CONCLUSIONS

The present model addresses wettability by the modification of the surface tension force at the contact line and not by minimizing the energy associated to contact areas. This is congruent with Gao and McCarthy [30] observations, who showed experimentally that contact lines, and not contact areas, are relevant in determining wettability. The newly derived phase-field model allows for predicting steady-state compact solutions such as drops on a flat surfaces. Unsteady compact solutions such as drops in pearling states are only possible due to a delicate balance between wetting dynamics and energy dissipation at the fluid-wall interface. The present model constitutes a quantitative tool to study wetting phenomena under several conditions. The introduction of a wall phase field allows for including, in a simplified

manner, complex surface morphologies. The model correctly reproduces static configurations defined by an equilibrium contact angle. Comparison with analytical solutions shows that the present model is highly accurate, despite the use of coarse meshes compared to traditional phase-field models. The use of the resharpening equation is the main reason for the good accuracy in the results.

Simulations of a spreading drop for fluids with high property contrast revealed a good agreement with the spreading dynamics observed experimentally by Quéré *et al.* for the inertia [$r(t) \propto t^{0.5}$] and dissipation [$r(t) \propto t^{0.1}$] controlled regimes. For fluids with identical properties, the simulations unveiled a quite interesting scaling law for the dissipation rate, which is close agreement to that predicted by the Kolmogorov's time scale. For fluids with high property contrast, the scaling law for the dissipation rate differs substantially, confirming that the dissipation mechanisms between single- and two-phase flows are quite distinctive.

The results for droplets on microstructured surfaces suggest that the wetting transition depends not only on the characteristics of the surface but also on the droplet size (R). If the surface is decorated with an square array of pillars separated by a distance d , then the transition is observed for a critical ratio between the droplet size and d through $\chi_c = R_c/d$. The simulations also infer a possible dependence on the pillars' height, but this was not confirmed. In addition, the droplet deposition might also have an important effect on the droplet behavior, as seen experimentally by Callies *et al.* [34].

For droplets impacting or sliding on a solid wall, the simulations revealed that the microscopic effects of an increased liquid viscosity close to the wall and the contact line pinning on surface defects can be accounted for by using an effective viscosity, controlled by β . Nonetheless, this coefficient only affects the dynamics of the contact line and not static configurations. For instance, the current model underpredicts the critical inclination angle for the onset of motion of droplets, which might be better captured by fully resolving the forces at the contact line on rough surfaces.

In spite of the good results obtained with the current model, further developments are still needed to treat broader types of problems. For instance, quantitative simulations of slowly evaporating water droplets in an open atmosphere require the addition of several concentration fields to account for all the species present in air and liquid water. In addition, disjoining pressure and possible effects of thermal fluctuations at the contact line or liquid-vapor interface have not been accounted for, but developments in that direction are currently ongoing.

ACKNOWLEDGMENTS

This work was supported by a grant from the Swiss National Supercomputing Centre (CSCS) under project ID psi.

APPENDIX A: DERIVATION OF THE NORMAL VECTOR

The normal vector used in the present model is defined as $\mathbf{n}_{lv} = \mathbf{r}_{lv}/|\mathbf{r}_{lv}|$. This vector is obtained by applying the gradient to the normalized liquid phase field, that is,

$$\nabla \left(\frac{\phi_l}{\phi_f} \right) = \frac{1}{\phi_f} \nabla \phi_l - \frac{\phi_l}{\phi_f^2} \nabla \phi_f. \quad (\text{A1})$$

By applying volume conservation $\phi_f = \phi_l + \phi_v$, we have

$$\nabla \left(\frac{\phi_l}{\phi_f} \right) = \frac{(\phi_l + \phi_v) \nabla \phi_l - \phi_l \nabla (\phi_l + \phi_v)}{\phi_f^2}, \quad (\text{A2})$$

which reduces finally to

$$\nabla \left(\frac{\phi_l}{\phi_f} \right) = \frac{\phi_v \nabla \phi_l - \phi_l \nabla \phi_v}{\phi_f^2}. \quad (\text{A3})$$

To properly calculate the normal vector for the liquid-vapor interface, even inside the three-phase region (contact line), we can define it in terms on the normalized liquid phase field as

$$\mathbf{n}_{lv} = \frac{\nabla \left(\frac{\phi_l}{\phi_f} \right)}{|\nabla \left(\frac{\phi_l}{\phi_f} \right)|}, \quad (\text{A4})$$

which is equivalent to

$$\mathbf{n}_{lv} = \frac{\mathbf{r}_{lv}}{|\mathbf{r}_{lv}|} \quad (\text{A5})$$

if $\mathbf{r}_{lv} = \phi_v \nabla \phi_l - \phi_l \nabla \phi_v$.

APPENDIX B: DERIVATION OF THE TRANSFORMATION POTENTIAL

$$\Pi_1 = \int_{\Omega} f(\phi_l, \phi_v, \nabla \phi_l, \nabla \phi_v) d\Omega, \quad (\text{B1})$$

where the free-energy density is defined as

$$f = -p_{eq} + 16\Delta f_{max} \frac{\phi_l^2 \phi_v^2}{\phi_f^4} + \frac{1}{2} \lambda_{PF}(z, \phi_w) \frac{|\mathbf{r}_{lv}|^2}{\phi_f^4}. \quad (\text{B2})$$

Here the equilibrium pressure p_{eq} only depends on temperature. The transformation potential for each phase reads

$$\mu_i = \frac{\partial f}{\partial \phi_i} - \nabla \cdot \left(\frac{\partial f}{\partial \nabla \phi_i} \right), \quad (\text{B3})$$

The transformation potential for the liquid-vapor interface is given by the difference between the potentials for each individual phase, that is,

$$\mu_{lv} = \frac{\partial f}{\partial \phi_l} - \frac{\partial f}{\partial \phi_v} - \nabla \cdot \left(\frac{\partial f}{\partial \nabla \phi_l} \right) + \nabla \cdot \left(\frac{\partial f}{\partial \nabla \phi_v} \right), \quad (\text{B4})$$

$$\begin{aligned} \frac{\partial f}{\partial \phi_l} - \frac{\partial f}{\partial \phi_v} &= 16\Delta f_{max} \frac{2\phi_l \phi_v (\phi_v - \phi_l)}{\phi_f^4} \\ &\quad + \frac{1}{2} \left(\frac{\partial \lambda_{lv}}{\partial \phi_l} - \frac{\partial \lambda_{lv}}{\partial \phi_v} \right) \frac{|\mathbf{r}_{lv}|^2}{\phi_f^4} \\ &\quad + \frac{\lambda_{lv} \mathbf{r}_{lv}}{\phi_f^4} \cdot \left(\frac{\partial \mathbf{r}_{lv}}{\partial \phi_l} - \frac{\partial \mathbf{r}_{lv}}{\partial \phi_v} \right) \end{aligned} \quad (\text{B5})$$

and

$$\frac{\partial f}{\partial \nabla \phi_l} - \frac{\partial f}{\partial \nabla \phi_v} = \frac{\lambda_{lv} \mathbf{r}_{lv}}{\phi_f^4} \left(\frac{\partial \mathbf{r}_{lv}}{\partial \nabla \phi_l} - \frac{\partial \mathbf{r}_{lv}}{\partial \nabla \phi_v} \right). \quad (\text{B6})$$

Since λ_{lv} is not a function of ϕ_l or ϕ_v , its partial derivatives respect to ϕ_l and ϕ_v are zero. Nonetheless, λ_{lv} could still be considered a function of the distance from the wall to account

for a possible variation of the surface tension in the proximity of the wall.

From the definition of $\mathbf{r}_{lv} = \phi_v \nabla \phi_l - \phi_l \nabla \phi_v$ and applying the definition for the fluid phase field $\phi_f = \phi_l + \phi_v$, we have

$$\frac{\partial \mathbf{r}_{lv}}{\partial \phi_l} - \frac{\partial \mathbf{r}_{lv}}{\partial \phi_v} = -\nabla \phi_f. \quad (\text{B7})$$

Since the volume fraction for the wall and fluid must satisfy volume conservation ($\phi_f + \phi_w = 1$) we have

$$\frac{\partial \mathbf{r}_{lv}}{\partial \phi_l} - \frac{\partial \mathbf{r}_{lv}}{\partial \phi_v} = \nabla \phi_w. \quad (\text{B8})$$

In addition,

$$\frac{\partial \mathbf{r}_{lv}}{\partial \nabla \phi_l} - \frac{\partial \mathbf{r}_{lv}}{\partial \nabla \phi_v} = \phi_f. \quad (\text{B9})$$

Thus the potential becomes

$$\begin{aligned} \mu_{lv} = 16\Delta f_{\max} & \frac{2\phi_l \phi_v (\phi_v - \phi_l)}{\phi_f^4} + \frac{\lambda_{lv} \mathbf{r}_{lv} \cdot \nabla \phi_w}{\phi_f^4} \\ & - \nabla \cdot \left(\frac{\lambda_{lv} \mathbf{r}_{lv}}{\phi_f^3} \right). \end{aligned} \quad (\text{B10})$$

$$\begin{aligned} \mu_{lv} \phi_f^4 = 16\Delta f_{\max} & 2\phi_l \phi_v (\phi_v - \phi_l) - \lambda_{lv} \phi_f \nabla \cdot \mathbf{r}_{lv} \\ & - 2\lambda_{lv} \mathbf{r}_{lv} \cdot \nabla \phi_w - \phi_f \mathbf{r}_{lv} \cdot \nabla \lambda_{lv}. \end{aligned} \quad (\text{B11})$$

By applying the definitions relating Δf_{\max} and λ_{lv} to the surface tension σ and interface thickness W provided by Badillo [24]

$$\begin{pmatrix} \lambda_{PF} \\ \Delta f_{\max} \end{pmatrix} = \begin{pmatrix} 4\sigma W/I_0 \\ \sigma/4WI_0 \end{pmatrix}, \quad (\text{B12})$$

we arrive at the final expression of the transformation potential given in Eq. (10).

APPENDIX C: CALCULATION OF THE DYNAMIC CONTACT ANGLE

To calculate the contact angle, the normalized liquid phase field $\phi_l^* = \phi_l/\phi_f$ was used. In a uniform grid represented by (i, j) indexes, the position of the fluid wall was first determined by finding the cells where $(2\phi_{wi,j} - 1)(2\phi_{wi,j-1} - 1) < 0$. Here the j index varies along the wall normal direction. Once the position of the fluid-wall interface was found, the position of the liquid-vapor interface along the i direction was determined for the next two consecutive rows ($j+1$ and $j+2$). This was accomplished by finding the cells where $(2\phi_{li,j+1}^* - 1)(2\phi_{li,j+1}^* - 1) < 0$ and $(2\phi_{li,j+2}^* - 1)(2\phi_{li,j+2}^* - 1) < 0$. The accurate location of the interface was found by a linear interpolation in the cells satisfying the previous three inequalities. If the interface position in the i direction differs by $\delta_{xi} = x_{\text{interface}}(j+2) - x_{\text{interface}}(j+1)$, the contact angle is simple obtained by $\theta_d = \arctan(\Delta y/\delta_{xi})$

-
- [1] D. Bonn, J. Eggers, J. Indekeu, J. Meunier, and E. Rolley, Rev. Mod. Phys. **81**, 739 (2009).
 - [2] Y. Sui, H. Ding, and P. D. Spelt, Annu. Rev. Fluid Mech. **46**, 97 (2014).
 - [3] R. G. Cox, J. Fluid Mech. **168**, 169 (1986).
 - [4] T. Qian, X.-P. Wang, and P. Sheng, Phys. Rev. E **68**, 016306 (2003).
 - [5] T. Qian, X.-P. Wang, and P. Sheng, Phys. Rev. Lett. **93**, 094501 (2004).
 - [6] D. M. Anderson, G. B. McFadden, and A. A. Wheeler, Annu. Rev. Fluid Mech. **30**, 139 (1998).
 - [7] P. Seppecher, Int. J. Eng. Sci. **34**, 977 (1996).
 - [8] L. Cueto-Felgueroso and R. Juanes, Phys. Rev. Lett. **108**, 144502 (2012).
 - [9] P. Yue and J. J. Feng, Phys. Fluids **23**, 012106 (2011).
 - [10] R. Teshigawara and A. Onuki, Phys. Rev. E **82**, 021603 (2010).
 - [11] R. Borcia, I. D. Borcia, and M. Bestehorn, Eur. Phys. J. Spec. Top. **166**, 127 (2009).
 - [12] M. Queralt-Martín, M. Pradas, R. Rodríguez-Trujillo, M. Arundell, E. Corvera Poiré, and A. Hernández-Machado, Phys. Rev. Lett. **106**, 194501 (2011).
 - [13] S. Guo, M. Gao, X. Xiong, Y. J. Wang, X. Wang, P. Sheng, and P. Tong, Phys. Rev. Lett. **111**, 026101 (2013).
 - [14] J. W. Cahn, J. Chem. Phys. **66**, 3667 (1977).
 - [15] W. Villanueva, W. Boettinger, G. McFadden, and J. Warren, Acta Mater. **60**, 3799 (2012).
 - [16] W. Villanueva, W. Boettinger, J. Warren, and G. Amberg, Acta Mater. **57**, 6022 (2009).
 - [17] W. Villanueva, K. Grönhagen, G. Amberg, and J. Ågren, Phys. Rev. E **77**, 056313 (2008).
 - [18] D. Wheeler, J. A. Warren, and W. J. Boettinger, Phys. Rev. E **82**, 051601 (2010).
 - [19] E. J. Schwalbach, S. H. Davis, P. W. Voorhees, J. A. Warren, and D. Wheeler, J. Appl. Phys. **111**, 024302 (2012).
 - [20] E. J. Schwalbach, S. H. Davis, P. W. Voorhees, D. Wheeler, and J. A. Warren, J. Mater. Res. **111**, 024302 (2012).
 - [21] A. A. Wheeler and G. B. McFadden, Proc Roy. Soc. Lond. Ser. A: Math., Phys. Eng. Sci. **453**, 1611 (1997).
 - [22] H. Garcke, B. Nestler, and B. Stoth, SIAM J. Appl. Math. **60**, 295 (1999).
 - [23] B. Nestler and A. Wheeler, Physica D **138**, 114 (2000).
 - [24] A. Badillo, Phys. Rev. E **86**, 041603 (2012).
 - [25] B. M. Mognetti and J. M. Yeomans, Langmuir **26**, 18162 (2010).
 - [26] D. Sibley, A. Nold, N. Savva, and S. Kalliadasis, Eur. Phys. J. E **36**, 26 (2013).
 - [27] G. Whyman, E. Bormashenko, and T. Stein, Chem. Phys. Lett. **450**, 355 (2008).
 - [28] N. Welzel, Ind. Eng. Chem. **28**, 988 (1936).
 - [29] A. B. D. Cassie and S. Baxter, Trans. Faraday Soc. **40**, 546 (1944).
 - [30] L. Gao and T. J. McCarthy, Langmuir **23**, 3762 (2007).
 - [31] I. Steinbach, F. Pezzolla, B. Nestler, M. Seelberg, R. Prieler, G. Schmitz, and J. Rezende, Physica D **94**, 135 (1996).
 - [32] A. Badillo, in *Proceedings of the ASME 2013 International Mechanical Engineering Congress and Exposition, San Diego* (ASME, New York, 2013).

- [33] B. Niceno, Y. Sato, A. Badillo, and M. Andreani, Nucl. Eng. Technol. **42**, 620 (2010).
- [34] M. Callies and D. Quere, Soft Matter **1**, 55 (2005).
- [35] S. Zahedi, K. Gustavsson, and G. Kreiss, J. Comput. Phys. **228**, 6361 (2009).
- [36] Y. Sato and B. Ničeno, J. Comput. Phys. **231**, 3887 (2012).
- [37] W. Villanueva and G. Amberg, Int. J. Multiphase Flow **32**, 1072 (2006).
- [38] A.-L. Biance, C. Clanet, and D. Quéré, Phys. Rev. E **69**, 016301 (2004).
- [39] N. Le Grand, A. Daerr, and L. Limat, J. Fluid Mech. **541**, 293 (2005).
- [40] Y. Y. Koh, Y. C. Lee, P. H. Gaskell, P. K. Jimack, and H. M. Thompson, Eur. Phys. J. Spec. Top. **166**, 117 (2009).
- [41] H. Huang and P. Meakin, Water Resour. Res. **44**, W03411 (2008).
- [42] N. R. Tas, J. Haneveld, H. V. Jansen, M. Elwenspoek, and A. van den Berg, Appl. Phys. Lett. **85**, 3274 (2004).
- [43] K. Yokoi, D. Vadillo, J. Hinch, and I. Hutchings, Phys. Fluids **21**, 072102 (2009).

Copyright of Physical Review E: Statistical, Nonlinear & Soft Matter Physics is the property of American Physical Society and its content may not be copied or emailed to multiple sites or posted to a listserv without the copyright holder's express written permission. However, users may print, download, or email articles for individual use.